Title: Activation and Evasion of the FEAR Pathway by RNA Viruses

Short title: RNA viruses and the FEAR Pathway

Emily A. Rex[1], Dahee Seo[1], Aaron Embry[1], Rozanne Arulanandam[2,3], Marcus M. Spinelli[2,3], Jean-Simon Diallo[2,3], and Don B. Gammon[1]*.

[1]Department of Microbiology, University of Texas Southwestern Medical Center, Dallas, TX, 75390, USA
[2]Center for Innovative Cancer Research, Ottawa Hospital Research Institute, 501 Smyth Road, Ottawa, Ontario K1H 8L6, Canada.
[3]Department of Biochemistry, Microbiology and Immunology, Faculty of Medicine, University of Ottawa, 451 Smyth Road, Ottawa, Ontario K1H 8M5, Canada.
*Corresponding author: Don B. Gammon. Contact: don.gammon@utsouthwestern.edu

Abstract

We recently identified the FACT-ETS-1 Antiviral Response (FEAR) pathway as an interferon-independent innate immune response that restricts DNA virus replication and is countered by poxvirus-encoded A51R proteins (Rex *et al.*, 2024, *Nature Microbiology*). The human FEAR pathway is mediated by the FACT complex, consisting of hSpt16 and SSRP1 subunits, that remodels chromatin to activate expression of the antiviral transcription factor, ETS-1. To counter this pathway, poxvirus A51R proteins tether SUMOylated hSpt16 subunits to microtubules to prevent ETS-1 expression. While these observations indicate a role for the FEAR pathway in DNA virus restriction, it was unclear if RNA viruses interact with this pathway. Here, we show that RNA viruses are also restricted by the FEAR pathway, yet encode mechanisms distinct from poxviruses to counter this response. We show vesicular stomatitis virus (VSV), a rhabdovirus, utilizes its matrix (M) protein to promote proteasome-dependent degradation of SUMOylated hSpt16 and to block ETS-1 nuclear import. Strains encoding mutant M proteins that cannot antagonize the FEAR pathway exhibit replication defects in human cells that can be rescued by hSpt16 or ETS-1 depletion. Moreover, FACT inhibitor treatment enhanced the replication of oncolytic VSV strains encoding defective M proteins in restrictive cancer cells, suggesting FEAR pathway inhibition may improve

oncolytic virotherapy. Strikingly, we provide evidence that the inability of VSV M to degrade SUMOylated Spt16 in lepidopteran insect cells results in abortive infection, suggesting VSV-Spt16 interactions influence virus host range. Lastly, we show that human and murine paramyxovirus target SUMOylated Spt16 proteins for degradation in human and murine cells utilizing a conserved N-terminal motif in their accessory "C" proteins. Collectively, our study illustrates that DNA and RNA viruses have independently evolved diverse mechanisms to antagonize SUMOylated host Spt16 proteins, underscoring the physiological importance of the FEAR pathway to antiviral immunity.

Keywords: FACT complex; ETS-1; FEAR pathway; RNA virus; viral immune evasion

Abbreviations

FACT-ETS-1 Antiviral Response (FEAR); vesicular stomatitis virus (VSV); matrix (M); interferon (IFN); facilitates chromatin transcription (FACT); vaccinia virus (VV); suppressor of Ty 16 homologue (Spt16); human Spt16 (hSpt16); SUMOylated hSpt16 ($hSpt16^{SUMO}$); structure specific recognition protein 1 (SSRP1); E26 transformation-specific sequence-1 (ETS-1); Ran GTPase activating protein (RanGAP); ribonucleic acid export 1 (Rae1); nucleoporin 98 (Nup98); nonsegmented negative-strand (NNS); *Lymantria dispar* Spt16 (LdSpt16); SUMOylated LdSpt16 ($LdSpt16^{SUMO}$); firefly luciferase (LUC); Sendai virus (SeV); Human parainfluenza virus-1 (HPIV-1).

52 **Introduction**

53

54 The activation of transcription-dependent responses during infection is a fundamental
55 aspect of eukaryotic antiviral immunity. In turn, evolutionary pressures on viruses to
56 efficiently replicate in their eukaryotic hosts have driven the acquisition of viral
57 countermeasures to these host responses [1-3]. Perhaps the strongest evidence for the
58 importance of an innate immune response pathway to combating infection is the
59 identification of pathogen-encoded antagonists of that pathway. The fact that virtually all
60 mammalian viruses encode antagonists of the Type I interferon (IFN) response
61 highlights the importance of this antiviral pathway [3-5]. However, relatively little is
62 known regarding IFN-independent transcriptional response pathways that restrict virus
63 replication and the mechanisms used by viruses to thwart such responses.

64

65 We recently reported the discovery of an IFN-independent "FACT-ETS-1 Antiviral
66 Response (FEAR)" pathway that requires the cellular Facilitates Chromatin Transcription
67 (FACT) complex for activation [6]. FACT is an ancient chromatin remodeling factor that
68 is conserved from yeast to humans. In humans, FACT is comprised of human
69 suppressor of ty 16 homologue (hSpt16) and structure specific recognition protein 1
70 (SSRP1) subunits that regulate cellular gene transcription by assembling and
71 disassembling nucleosomes at specific loci [7, 8]. Using vaccinia virus (VV), a large DNA
72 virus belonging to the *Poxviridae* family, we showed that viral infection triggers the
73 FACT-dependent expression of E26 transformation-specific sequence-1 (ETS-1), an
74 antiviral transcription factor, which subsequently promotes VV restriction [6]. ETS-1
75 expression during infection is dependent upon FACT complexes that contain a
76 specialized, SUMOylated form of hSpt16 ($hSpt16^{SUMO}$)[6]. However, we found the VV-

77 encoded A51R protein to block ETS-1 expression by outcompeting SSRP1 for direct
78 binding to hSpt16^{SUMO} subunits in the cytosol and by tethering hSpt16^{SUMO} to
79 microtubules [6]. VV mutant strains lacking A51R or encoding A51R mutants unable to
80 bind hSpt16^{SUMO} strongly induce ETS-1 expression and display attenuated replication in
81 human cell culture and in mice, suggesting the FEAR pathway is a critical component of
82 eukaryotic antiviral immunity and that poxvirus A51R proteins function as FEAR pathway
83 antagonists [6].
84
85 Prior to our identification of the FEAR pathway, we had serendipitously discovered that
86 poxvirus A51R proteins could rescue the abortive infection of lepidopteran (moth and
87 butterfly) cells by vesicular stomatitis virus (VSV), a small RNA virus belonging to the
88 *Rhabdoviridae* family [9]. Although VSV is an arbovirus and can be naturally transmitted
89 by blood-feeding dipteran (flies and mosquitoes) insects to mammalian hosts,
90 lepidopterans are unnatural hosts for this virus. Thus, we suspected that A51R proteins
91 may promote productive VSV replication in lepidopteran cells by suppressing an immune
92 response that VSV is incapable of evading in these host cells [9]. Given that A51R
93 proteins are only encoded by vertebrate poxviruses [9], we suspected that these viral
94 proteins are likely immunosuppressive in insect cells because they target antiviral
95 machinery conserved between invertebrate and vertebrate hosts. However, the nature of
96 the host response restricting VSV and suppressed by A51R has remained elusive.
97
98 Understanding innate immune responses restricting VSV replication is important for
99 many reasons. For one, VSV it is associated with outbreaks in livestock in the United
100 States and thus poses a significant economic burden to the agriculture industry [10].
101 Moreover, the early development of a reverse genetic system for VSV [11, 12], its ability

102 to infect a broad range of host cell types [13], and inability to cause significant disease in
103 humans [14], have made VSV an important model for understanding fundamental
104 aspects of nonsegmented negative-strand (NNS) RNA virus biology. VSV has also
105 become an important vaccine platform for a wide variety of other viral diseases [14, 15].
106
107 VSV is also being investigated as an oncolytic agent in basic and clinical studies [16,
108 17]. A rapid and lytic replication cycle, and lack of preexisting immunity in the human
109 population to VSV, are key advantages of its use in oncolytic virotherapy. Oncolytic VSV
110 strains encoding either a deletion or Arg substitution at Met51 in the VSV M protein
111 ($VSV^{\Delta M51}$ and VSV^{M51R}) have been widely studied in oncolytic virotherapy [16-23]. These
112 strains typically display attenuated replication due to their reduced ability to block host
113 gene expression, although how wild-type VSV M normally impedes cellular gene
114 expression is controversial [24, 25]. Prior work has shown that antiviral gene expression
115 by the IFN response is antagonized by wild-type, but not $VSV^{\Delta M51}$ or VSV^{M51R} strains [16-
116 19]. It has been suggested that the reduced ability of $VSV^{\Delta M51}$ and VSV^{M51R} strains to
117 replicate in untransformed cells may be due to defective IFN antagonism [18, 21, 25,
118 26]. However, in transformed cells, the IFN pathway is often defective because this
119 pathway can also activate anti-proliferative and pro-death responses that would be
120 detrimental to cancer cell replication and survival [27]. Thus, part of the selectivity of
121 $VSV^{\Delta M51}$ and VSV^{M51R} strains for replication in cancer cells may be in part due to
122 defective IFN signaling in these cells. However, not all transformed cells are IFN-
123 defective, possibly explaining why some cancer cell types are refractory to oncolytic VSV
124 strains [18, 21, 23]. Indeed, prior work has shown that certain cancer cell lines that are
125 refractory to $VSV^{\Delta M51}$ replication can become sensitized to infection by treatment with
126 compounds that inhibit IFN responses [18, 21]. However, it is unclear if IFN-independent

127 responses also contribute to VSV$^{\Delta M51}$ and VSV^{M51R} restriction in refractory cancer cell
128 types. Thus, identifying and overcoming innate immune responses present in cancer
129 cells that restrict oncolytic VSV strain replication is critical for improving virotherapy
130 because enhanced VSV replication is associated with increased oncolysis and improved
131 virotherapy outcomes [18, 20, 21, 28, 29].
132
133 Interestingly, upregulation of FACT and ETS-1 have been linked to oncogenesis and/or
134 tumor invasion [30-32]. For example, FACT subunit upregulation is strongly associated
135 with aggressive tumor types [31], suggesting that FACT can drive oncogenic gene
136 expression programs that favor cancer development. This led to the development of
137 small molecule inhibitors of FACT called “curaxins” that are currently being pursued in
138 clinical trials for the treatment of human malignancies [33]. ETS-1 is a proto-oncoprotein
139 and its upregulation promotes cellular transformation and tumor invasion [30, 34]. These
140 observations suggest that the FEAR pathway involves host factors that are both antiviral
141 and pro-tumoral. Thus, if the FEAR pathway is retained in transformed cells, it may be
142 relevant to the restriction of oncolytic viruses and thus blocking this pathway with FACT
143 inhibitors such as curaxins may be a logical strategy to improve the oncolytic virus
144 replication.
145
146 With our discovery of poxvirus A51R proteins as the first DNA virus-encoded FEAR
147 pathway antagonists [6], we wanted to use VSV as a model to investigate if RNA viruses
148 activate and/or antagonize this pathway. Here, we show that the attenuated replication
149 of VSV$^{\Delta M51}$/VSV^{M51R} strains is at least in part due their inability to suppress FEAR
150 pathway activation in human cells. In contrast, VSV strains encoding wild-type M
151 proteins effectively suppress this pathway by promoting the proteasome-dependent

152 degradation of hSpt16^{SUMO} to abrogate ETS-1 expression and by blocking ETS-1 nuclear
153 accumulation. We find that inhibition of the FEAR pathway in human cancer lines
154 normally resistant to VSV$^{\Delta M51}$/VSV^{M51R} infection by hSpt16 RNA interference (RNAi) or
155 curaxin treatment sensitizes these cancer cells to infection with these oncolytic viruses.
156 Moreover, we show that the host range restriction of VSV in lepidopteran cells likely
157 results from an inability of VSV M to degrade SUMOylated Spt16 proteins encoded by
158 these insect hosts. Our data suggests that VV A51R rescues this VSV host range
159 restriction by interacting with SUMOylated Spt16 expressed in these insect cells. Finally,
160 we show that murine and human paramyxovirus-encoded C proteins target SUMOylated
161 Spt16 proteins for proteasomal degradation in mouse and human cells using a
162 conserved motif in their N-termini, suggesting that other NNS RNA viruses have
163 independently evolved strategies to degrade these host factors. Collectively, our work
164 illustrates that RNA viruses can also activate and antagonize the FEAR pathway and, to
165 our knowledge, identifies VSV M and paramyxovirus C proteins as the first RNA virus-
166 encoded FEAR pathway antagonists.
167

168 ## Results

169

170 **hSpt16 or ETS-1 depletion rescues the replication defect of a VSV^{M51R} mutant**

171

172 We previously showed that hSpt16 RNAi significantly enhances the replication of VSV in
173 both A549 cells and primary neonatal human dermal fibroblasts, suggesting that FACT
174 contributes to VSV restriction [6]. However, we wanted to ask if ETS-1 was also
175 restrictive to VSV replication because it was possible that FACT-mediated VSV
176 restriction is independent of ETS-1. Moreover, because VSV$^{\Delta M51}$ or VSV^{M51R} strains are

177 thought to exhibit replication defects because of their inability to block host gene
178 expression-dependent antiviral responses, we wondered whether these replication
179 defects may be related to a differential ability of these mutant viruses to antagonize the
180 FEAR pathway.
181
182 To begin to address these questions, we assessed the replication of recombinant VSV
183 strains encoding eGFP and either wild-type (VSV-eGFP) [35] or M51R mutant M
184 (VSV^{M51R}-eGFP) proteins [35] in A549 cells transfected with small interfering RNAs
185 (siRNAs) targeting hSpt16 or ETS-1 [6]. We found hSpt16 or ETS-1 RNAi to significantly
186 enhance VSV-eGFP replication compared to scrambled (control) RNAi conditions,
187 suggesting the FEAR pathway is indeed restrictive to VSV. The VSV^{M51R}-eGFP strain
188 exhibited a replication defect compared to VSV-eGFP under control RNAi conditions but
189 strikingly, under either hSpt16 or ETS-1 RNAi conditions, this mutant replicated to titers
190 indistinguishable from VSV-eGFP (**Fig 1A and B**). These results suggest that the FEAR
191 pathway contributes to VSV restriction and that the VSV^{M51R}-eGFP mutant strain is more
192 sensitive to restriction by this pathway.
193
194 **Wild-type VSV, but not VSV^{M51R}, inhibits ETS-1 expression to evade restriction**
195
196 The results above were reminiscent of our VV studies where we found a VV strain
197 lacking A51R (ΔA51R) to exhibit a replication defect that could be rescued by FACT
198 subunit or ETS-1 depletion. We also found this ΔA51R strain to more strongly induce
199 ETS-1 expression than wild-type VV [6]. Thus, we next used infection time courses and
200 immunoblots (IBs) to determine if ETS-1 levels differ between VSV-eGFP and VSV^{M51R}-
201 eGFP infections. Interestingly, while ETS-1 protein levels were not significantly different

202 between mock- and VSV-eGFP-infected cells, VSV^{M51R}-eGFP-infected WCE showed
203 significantly elevated ETS-1 by 4 h post-infection (hpi) (**Fig 1C and D**). These results
204 indicate that infection with the VSV^{M51R}-eGFP mutant induces ETS-1 expression while
205 wild-type (VSV-eGFP) infection does not induce ETS-1.
206
207 We hypothesized that wild-type VSV suppresses ETS-1 expression to prevent activation
208 of antiviral gene expression programs that require elevated ETS-1 levels. Therefore, we
209 next asked if ETS-1 overexpression prior to infection could suppress VSV-eGFP
210 infection. To do this, we overexpressed an HA-tagged human ETS-1 construct (ETS-1-
211 HA) in cells for 48 h (**Fig 1E**) and then challenged cells with VSV-eGFP. Using
212 fluorescence microscopy, we quantified GFP signals as a readout for infection and
213 normalized these signals to total cell number by labeling cell nuclei with NucBlue.
214 Compared to cultures transfected with empty vector (control), ETS-1-HA-transfected
215 cells displayed significantly reduced GFP signal (**Fig 1F and G**). Collectively, these data
216 suggest ETS-1 expression results in a block to VSV infection but VSV-eGFP evades this
217 restriction by suppressing ETS-1 expression. In contrast, VSV^{M51R}-eGFP is unable to
218 block ETS-1 induction.
219
220 **VSV^{M51R} infection induces ETS-1 expression independently of RIG-I and the IFN**
221 **response**
222
223 We showed ΔA51R VV strains to induce ETS-1 expression in the absence of an intact
224 IFN response [6]. Therefore, we wanted to determine if ETS-1 induction by VSV^{M51R}-
225 eGFP infection was also independent of the IFN response. Since the pattern recognition
226 receptor RIG-I is required for the activation of IFN responses during VSV infection of

227 non-immune cell types [36], we first examined ETS-1 induction in RIG-I-deficient A549
228 cells. No significant differences in ETS-1 induction were found between wild-type and
229 RIG-I knockout cells during VSV^{M51R}-eGFP infection (**Fig S1A and B**). We also
230 quantified ETS-1 expression levels in A549 cells lacking IRF3 or STAT1, two critical
231 components of the IFN signaling pathway [37, 38]. ETS-1 induction by VSV^{M51R}-eGFP
232 infection was unaffected in these IFN pathway knockout cell lines (**Fig S1C-F**).
233 Collectively, these data indicate that, like VV, VSV activates ETS-1 expression
234 independently of the IFN response.
235
236 **VSV, but not VSV^{M51R}, promotes hSpt16^{SUMO} depletion to prevent ETS-1 induction**
237
238 During VV infection, FACT complexes comprised of hSpt16^{SUMO} and SSRP1 subunits
239 are required to induce ETS-1 expression [6]. Therefore, we hypothesized that VSV-
240 eGFP may suppress ETS-1 expression by altering FACT subunit levels. Using infection
241 time courses and IBs, we determined if hSpt16^{SUMO} or SSRP1 levels differ between
242 VSV-eGFP and VSV^{M51R}-eGFP infections. It is important to note that both hSpt16^{SUMO}
243 and SUMOless hSpt16 forms can be resolved from one another by SDS-PAGE using
244 low percentage acrylamide protein gels and then simultaneously detected via IB with
245 hSpt16 antibodies (Ab) [6]. Strikingly, our IBs revealed a clear and significant reduction
246 of hSpt16^{SUMO} (upper band in **Fig 2A**) levels compared to mock-infected WCE during
247 VSV-eGFP infection by 4 hpi and hSpt16^{SUMO} became virtually undetectable by 8 hpi. In
248 contrast, hSpt16^{SUMO} levels remained unchanged throughout the entire VSV^{M51R}-eGFP
249 infection time course (**Fig 2A and B**). Interestingly, SUMOless hSpt16 (lower band in
250 **Fig 2A**) or SSRP1 levels did not change during infection with either virus (**Fig 2C and**
251 **D**), suggesting that VSV infection leads to the specific depletion of hSpt16^{SUMO} subunits.

252 When comparing the effect of MOI on hSpt16^{SUMO} depletion during VSV-eGFP infection,
253 we noticed that complete depletion of hSpt16^{SUMO} levels occurred earlier (by 4 hpi) when
254 using higher MOIs (e.g. 10-30) versus during lower MOI (e.g. 3) infections. However, the
255 VSV^{M51R}-eGFP strain could not deplete hSpt16^{SUMO} at any MOI or time point (**Fig 2A**
256 **and S2)**.
257
258 To confirm these data, and to determine if loss of hSpt16^{SUMO} levels during VSV-eGFP
259 infection was not due to a global down regulation of intracellular SUMOylation, we used
260 Ab against SUMO-1 or SUMO-2/3 to immunoprecipitate (IP) SUMOylated protein
261 fractions from mock-, VSV-eGFP-, or VSV^{M51R}-eGFP-infected WCE [6]. As expected,
262 hSpt16^{SUMO} was specifically depleted in VSV-eGFP-infected WCE while present in
263 VSV^{M51R}-eGFP-infected lysates. Moreover, no overt reductions in either total
264 SUMOylation banding patterns or levels of SUMOylated-RanGAP1 (an abundant,
265 SUMOylated protein [39]) were observed in VSV-eGFP versus VSV^{M51R}-eGFP infections
266 (**Fig 2E and F**). These data suggest that VSV-eGFP can promote depletion of hSpt16
267 that is SUMOylated with either SUMO-1 or SUMO-2/3 and that the specific loss of
268 hSpt16^{SUMO} levels during VSV-eGFP infection is not due to a generalized decrease in
269 intracellular SUMOylation.
270
271 Finally, because hSpt16^{SUMO} is required for ETS-1 induction during ΔA51R VV infection
272 [6], we wanted to determine if hSpt16 RNAi treatment would inhibit ETS-1 induction by
273 VSV^{M51R}-eGFP infection. Consistent with our VV studies, hSpt16 RNAi treatment
274 abrogated ETS-1 induction after VSV^{M51R}-eGFP infection (**Fig 2G**). Collectively, these
275 data indicate that the inability of VSV^{M51R}-eGFP to deplete hSpt16^{SUMO} results in robust
276 ETS-1 induction during infection.

277

278 **VSV M is sufficient to promote proteasomal degradation of cytoplasmic**

279 **hSpt16^{SUMO} and to block ETS-1 expression**

280

281 Given that the only difference between VSV-eGFP and VSV^{M51R}-eGFP strains is the
282 M51R substitution in the VSV M protein, we hypothesized that this viral factor was
283 responsible for hSpt16^{SUMO} depletion. Consistent with this, a VSV$^{\Delta M51}$ strain expressing
284 GFP (VSV$^{\Delta M51}$-GFP [18]) was also unable to deplete hSpt16^{SUMO} levels when compared
285 to its wild-type VSV-GFP control strain (**Fig S3**). However, we still conducted a screen of
286 4 of the 5 VSV-encoded proteins to determine if any of these viral factors could reduce
287 hSpt16^{SUMO} levels when expressed from plasmids in uninfected human cells. The VSV L
288 protein, encoding the viral RNA polymerase, was excluded from this screen as it seemed
289 unlikely to be involved in immune evasion. Consistent with our hypothesis, only
290 expression of Flag-tagged VSV M (VSV M-Flag) resulted in hSpt16^{SUMO} depletion (**Fig**
291 **3A**). Moreover, expression of either VSV M$^{\Delta M51}$-Flag or VSV M^{M51R}-Flag mutant
292 constructs failed to deplete hSpt16^{SUMO} levels (**Fig 3B**), consistent with our infection
293 results. These data indicate that wild-type VSV M proteins, but not M51R or ΔM51
294 mutants, are sufficient for hSpt16^{SUMO} depletion in the absence of other VSV proteins.

295

296 VSV M can inhibit host gene expression by binding to Rae1, a component of the cellular
297 Rae1-Nup98 export complex that promotes mRNA export from the nucleus [25].
298 However, the mechanism by which VSV M-Rae1 interaction inhibits host gene
299 expression is controversial [24, 25]. In one proposed model, VSV M binds Rae1 to inhibit
300 Rae1-Nup98-mediated mRNA export from the nucleus while an alternative model
301 suggests VSV M may usurp Rae1-Nup98 complexes to inhibit cellular gene transcription

302 [24, 25]. Notably, VSV M51R/ΔM51 M mutants cannot interact with Rae1 [25]. Despite
303 the unresolved nature of VSV M-Rae1 interaction models, we wanted to determine if
304 Rae1 or Nup98 was involved in hSpt16^{SUMO} level regulation. Thus, we tested if depletion
305 of either Rae1 or Nup98 altered hSpt16^{SUMO} levels in mock-infected cells or inhibited
306 hSpt16^{SUMO} depletion during VSV-eGFP infection. In either case, we observed no effect
307 of Rae1 or Nup98 depletion on hSpt16^{SUMO} levels (**Fig S4**). This suggests that VSV M
308 antagonism of the FEAR pathway cannot be explained by its interaction with Rae1-
309 Nup98 complexes.
310
311 We next wanted to gain additional insight into the mechanism by which VSV M depletes
312 hSpt16^{SUMO} levels. Given that VV A51R blocks the FEAR pathway by binding to cytosolic
313 hSpt16^{SUMO} subunits, we next asked if VSV M also targets cytosolic hSpt16^{SUMO}
314 subunits. To do this, we co-expressed VSV M-Flag constructs with either a wild-type or
315 nuclear localization sequence (NLS)-deleted (NLS) HA-tagged hSpt16 constructs we
316 previously generated [6]. Importantly, we confirmed that wild-type HA-hSpt16 displayed
317 both cytosolic and nuclear localization while the HA-hSpt16$^{\Delta NLS}$ mutant was restricted to
318 the cytosol (**Fig 3C**). Upon co-transfection with wild-type VSV M-Flag, the SUMOylated
319 forms of both wild-type and NLS-deleted HA-hSpt16 constructs were depleted (**Fig 3D**),
320 indicating VSV M-Flag likely targets hSpt16^{SUMO} subunits in the cytoplasm. To determine
321 if VSV M promotes proteasome-dependent degradation of hSpt16^{SUMO}, we expressed
322 VSV M-Flag in human cells in the absence or presence of proteasome inhibitors
323 bortezomib or MG132 and assessed hSpt16^{SUMO} levels by IB. Interestingly, hSpt16^{SUMO}
324 depletion was blocked in the presence of either proteasome inhibitor (**Fig 3E and F**),
325 suggesting VSV M promotes the proteasome-dependent degradation of hSpt16^{SUMO}.
326

327 Finally, we asked if plasmid-based expression of VSV M-Flag was sufficient to block
328 ETS-1 induction by either VSV^{M51R}-eGFP (**Fig 3G and H**) or ∆A51R VV (**Fig 3I and J**)
329 infection. In both cases prior expression of VSV M-Flag, but not VSV M^{M51R}-Flag, was
330 able to suppress ETS-1 induction by either of these mutant viruses (**Fig 3G-J**). The
331 ability of VSV M to complement the ∆A51R strains inability to block ETS-1 expression
332 demonstrates VSV M is a bona fide FEAR pathway antagonist that can function
333 independently of other VSV proteins. Collectively, our prior and current findings suggest
334 that VV and VSV have independently evolved unique strategies to inhibit FACT-
335 dependent ETS-1 expression by either tethering hSpt16^{SUMO} to microtubules (VV A51R)
336 or by promoting hSpt16^{SUMO} degradation (VSV M), illustrating that FEAR pathway
337 suppression is important for both DNA and RNA viruses.
338
339 **VSV M encodes a second mechanism to inhibit ETS-1 function: blockade of**
340 **nuclear import**
341
342 While the specific antiviral function that ETS-1 performs after FEAR pathway activation
343 is still an active area of investigation, ETS-1 is known to regulate host transcription in the
344 nucleus. Thus, we determined if ETS-1 localizes to the nucleus during VSV infection.
345 First, we used immunofluorescence microscopy to examine endogenous ETS-1
346 localization in mock-, VSV-eGFP-, or VSV^{M51R}-eGFP-infected human A549 cells. In
347 mock-infected cells, both cytosolic and nuclear ETS-1 staining was observed, consistent
348 with the known nucleocytoplasmic cycling of ETS-1 [40, 41]. However, during VSV-
349 eGFP infection, ETS-1, was largely excluded from the nucleus and restricted to the
350 cytosol, suggesting that VSV infection impairs ETS-1 nuclear translocation. In contrast,
351 ETS-1 signals were stronger and predominantly nuclear in VSV^{M51R}-eGFP-infected cells

352 (**Fig 4A**). To complement our microscopy experiments, we conducted cell fractionation
353 and IB studies to quantify the percentage of total ETS-1 protein in nuclear fractions.
354 Consistent with our microscopy results, ~37% of total ETS-1 was found in nuclear
355 fractions of mock-infected cells, while only ~10% of ETS-1 was nuclear during VSV-
356 eGFP infection. In contrast, ~78% of ETS-1 was found in the nucleus during VSV^{M51R}-
357 eGFP infection (**Fig 4B and C**). Importantly, immunofluorescence experiments in U2OS
358 cells also demonstrated a similar exclusion of ETS-1 from the nucleus during VSV-eGFP
359 infections as observed in A549 cells (**Fig 4D**), suggesting this was not cell type-specific.
360 Finally, to determine if VSV M was able to impede ETS-1 nuclear localization in the
361 absence of other VSV proteins, we co-transfected the ETS-1-HA expression vector with
362 empty vector, VSV M-Flag, or VSV^{M51R}-Flag constructs into U2OS cells. In the presence
363 of empty vector or VSV^{M51R}-Flag constructs, ETS-1-HA displayed both nuclear and
364 cytosolic localization. However, in the presence of wild-type VSV M-Flag, ETS-1-HA
365 staining was largely excluded from the nucleus and restricted to the cytoplasm (**Fig 4E**).

366 Collectively, these data indicate that, during infection, ETS-1 accumulates in the nucleus
367 in the presence of the M51R mutant M protein but not in the presence of wild-type VSV
368 M. Moreover, our transfection experiments suggest VSV M can prevent ETS-1 nuclear
369 accumulation in the absence of other VSV proteins, indicating it encodes an additional
370 mechanism of antagonizing the FEAR pathway- blocking ETS-1 nuclear import.

371 **FEAR pathway inhibition enhances oncolytic VSV strain replication in refractory**
372 **cancer cells**

373

374 VSV$^{\Delta M51}$ and VSV^{M51R} viruses are being pursued for use in oncolytic virotherapy. While
375 effective at infecting some human cancer cell types, some transformed cell types have

376 proven to be refractory to infection by these oncolytic VSV strains, posing a major
377 challenge to their wide-spread use [18, 21, 23]. Thus, we asked if the FEAR pathway
378 may contribute to restriction of oncolytic VSV strain replication in human cancer lines
379 known to be refractory to $VSV^{\Delta M51}$/VSV^{M51R} viruses. First, we measured replication of
380 $VSV^{\Delta M51}$-GFP in human 786-0 renal adenocarcinoma cells, which are relatively resistant
381 to infection with this virus [18, 21], after hSpt16 RNAi. As shown in **Fig 5A**, $VSV^{\Delta M51}$-GFP
382 replication was significantly increased in 786-0 cells after hSpt16 depletion by RNAi.
383 Importantly, we confirmed that both hSpt16 and ETS-1 were reduced in 786-0 cells
384 infected with $VSV^{\Delta M51}$-GFP during hSpt16 knockdown (**Fig 5B**). These data suggest the
385 FEAR pathway contributes to the restriction of this virus in this restrictive cell type.

386 Since the use of hSpt16 RNAi as a therapeutic strategy to inhibit the FEAR pathway is
387 likely to be technically challenging *in vivo*, we conducted a "proof of principle" series of
388 cell culture experiments to determine if treatment with the small molecule FACT inhibitor,
389 CBL0137, could similarly enhance $VSV^{\Delta M51}$-GFP replication in restrictive cancer cell
390 types. CBL0137 is a second-generation curaxin and has broad activity against diverse
391 cancer cell types in culture and in mouse models and is being pursued in clinical trials as
392 a therapeutic for various malignancies [33, 42-45]. Curaxins inhibit FACT by causing this
393 complex to become trapped on chromatin, preventing it from functioning properly in gene
394 expression regulation [33]. First, we used quantitative fluorescence microscopy and GFP
395 signal as a simple readout of $VSV^{\Delta M51}$-GFP replication in 786-0 cells in the presence of a
396 broad range of CBL0137 concentrations 24 hpi. Addition of CBL0137 to media 1 hpi led
397 to a dose-dependent increase in GFP signal, peaking at an ~34-fold increase in GFP
398 signal with addition of 3 μM CBL0137 compared to infected cultures without curaxin (**Fig
399 5C and D, right axis**). We also analyzed cell viability via fluorometric resazurin assays

400 of parallel 786-0 cultures treated with either CBL0137 alone or VSV$^{\Delta M51}$-GFP+CBL0137
401 after 48 h and found a clear synergistic effect of the combined treatment on cancer cell
402 killing. For example, in cultures treated with 1.3 μM CBL0137 only, cell viability was
403 ~72% of untreated cultures. However, combining 1.3 μM curaxin with VSV$^{\Delta M51}$-GFP
404 treatment reduced 786-0 cell viability to ~10% of controls (**Fig 5D, left axis**). Importantly,
405 we verified that the increased GFP signal observed in CBL0137-treated cultures
406 correlated with elevated VSV$^{\Delta M51}$-GFP titers (**Fig 5E**) and with inhibition of ETS-1
407 expression (**Fig 5F**). We also tested the human melanoma cell line, RPMI 7951, which is
408 resistant to infection with VSV^{M51R} oncolytic strains [23] and observed enhanced
409 VSV$^{\Delta M51}$-GFP replication in these cells in the presence of CBL0137 (**Fig 5G**), suggesting
410 curaxin may sensitize other types of cancer cells to oncolytic VSV strain infection.
411 Collectively, these data suggest that hSpt16 depletion or FACT inhibition with curaxins
412 can enhance the replication of an oncolytic VSV strain lacking a functional FEAR
413 pathway antagonist in restrictive human cancer cell types.

414 **FACT contributes to VSV host range restriction in *Lymantria dispar* insect cells**

415

416 We originally became interested in understanding poxvirus A51R protein function after
417 discovering that these proteins rescue the post-entry abortive infection of VSV in
418 *Lymantria dispar* (gypsy moth or spongy moth)-derived LD652 cells [9]. With the
419 knowledge that VV A51R binds to hSpt16^{SUMO} to antagonize its antiviral function [6] and
420 that Spt16 proteins are conserved in all eukaryotes, we wondered if VV A51R-mediated
421 rescue of VSV in LD652 cells related to its ability to antagonize insect Spt16 function.

422

423 After sequencing the *L. dispar* genome [46], we discovered that hSpt16 and *L. dispar*
424 Spt16 (LdSpt16) proteins share an overall a.a. identity of ~60% [6]. However, alignment
425 of the A51R-binding domain in hSpt16 [6] with the corresponding region in LdSpt16
426 showed this region to be ~73% identical between these Spt16 proteins (**Fig S5**).
427 However, because VV A51R only binds SUMOylated forms of hSpt16, it was important
428 to determine if LdSpt16 was also SUMOylated. Interestingly, IBs of LD652 WCE
429 revealed two LdSpt16 forms as found with hSpt16 in human cells. Treatment of LD652
430 cultures with tannic acid, a global SUMOylation inhibitor [47], eliminated the upper
431 LdSpt16 form on IBs, suggesting this band represents SUMOylated LdSpt16
432 ($LdSpt16^{SUMO}$) (**Fig 6A**). To determine if VV A51R interacts with $LdSpt16^{SUMO}$, we
433 infected LD652 cells with a recombinant VV strain encoding Flag-tagged A51R (FA51R)
434 under its natural *A51R* gene promoter ($\Delta A51R^{FA51R}$) and then performed co-
435 immunoprecipitation [6]. Interestingly, $LdSpt16^{SUMO}$, but not SUMOless LdSpt16 proteins,
436 specifically co-immunoprecipitated with FA51R in LD652 WCE (**Fig 6B)**, suggesting VV
437 A51R can interact with SUMOylated Spt16 proteins in this insect host. Next, we tested if
438 A51R-LdSpt16 interactions were required for A51R-mediated rescue of VSV replication
439 in LD652 cells. To do this, we transfected LD652 cells with a control expression vector
440 encoding Flag-tagged GFP (FGFP) or vectors encoding wild-type FA51R, or a FA51R
441 mutant that cannot bind to SUMOylated Spt16 proteins $FA51R^{158\text{-}162Ala}$ [6]. 48 h post-
442 transfection, we challenged cells with a recombinant VSV strain encoding firefly
443 luciferase (VSV-LUC) [48]. We then assessed VSV-LUC gene expression with luciferase
444 assays and measured viral titers in collected LD652 culture supernatants [9]. While the
445 wild-type FA51R construct was able to rescue both VSV gene expression and
446 replication, the $FA51R^{158\text{-}162Ala}$ mutant was completely defective in this regard (**Fig 6C**

447 **and D**). These results suggest that VV A51R-mediated rescue of VSV requires A51R-
448 LdSpt16^{SUMO} interaction.

449 To directly test if LdSpt16 was involved in VSV restriction, we used *in vitro*-transcribed
450 dsRNAs to target LdSpt16 by RNAi. Compared to control RNAi targeting an irrelevant
451 GFP mRNA sequence, VSV-LUC gene expression (**Fig 6E**) and replication (**Fig 6F**)
452 were significantly enhanced in LD652 cultures transfected with dsRNAs targeting
453 LdSpt16 mRNA. These results suggested that the abortive infection of wild-type VSV in
454 LD652 cells is at least in part dependent upon LdSpt16^{SUMO}-mediated restriction.
455 Therefore, we hypothesized that wild-type VSV M may be defective in its ability to target
456 LdSpt16^{SUMO} for degradation. Consistent with this hypothesis, VSV M-Flag transfection
457 into LD652 cells failed to promote LdSpt16^{SUMO} depletion at any expression level tested
458 (**Fig 6G**). Collectively, these results suggest that VSV host range restriction in LD652
459 cells may be due to an inability of VSV M to antagonize LdSpt16^{SUMO} function.
460

461 **Paramyxovirus-encoded C proteins also promote proteasomal degradation of**
462 **hSpt16^{SUMO}**
463

464 Finally, we asked if other NNS RNA viruses, unrelated to VSV, also interact with the
465 FEAR pathway. We focused on viruses belonging to the *Paramyxoviridae* family
466 because they include important animal and human pathogens. For example, Sendai
467 virus (SeV) is a natural pathogen of rodents and a common cause of viral pneumonia in
468 wild and laboratory rodents [49]. Although not known to be pathogenic to humans, SeV
469 can productively replicate in human cells and has been an important model for
470 understanding paramyxovirus replication and immune evasion mechanisms [50, 51].

471 To determine if the FEAR pathway is relevant to paramyxovirus restriction, we
472 challenged A549 cells with a recombinant SeV strain encoding GFP (SeV-GFP) after
473 hSpt16 RNAi. Compared to control RNAi conditions, hSpt16 RNAi led to a significant
474 increase in SeV-GFP replication (**Fig 7A**), suggesting the FEAR pathway may also
475 restrict paramyxoviruses. We next examined if FACT subunit levels were altered during
476 SeV-GFP infection. Due to the slower replication cycle of SeV compared to VSV, we
477 collected WCE at relatively later time points (8 and 24 hpi). Interestingly, while FACT
478 subunit levels were largely unchanged at 8 hpi, hSpt16^{SUMO} subunits were specifically
479 eliminated in SeV-GFP-infected cells by 24 hpi, suggesting SeV encodes an antagonist
480 of hSpt16^{SUMO} (**Fig 7B**).

481 We suspected that the SeV-encoded accessory "C" proteins may be involved in
482 mediating hSpt16^{SUMO} depletion because they function as immune evasion factors [50].
483 During SeV infection, C proteins are expressed as a nested set of four different proteins
484 (C', C, Y1, and Y2) that derive from the same SeV *P* gene-derived mRNA and contain
485 common C-termini but differ in their N-termini due to the use of alternative translation
486 start sites [52-54] (**Fig 7C**). SeV C' is the largest of these four proteins so we first
487 examined if Flag-tagged SeV C' (SeV C'-Flag) expression could promote hSpt16^{SUMO}
488 depletion. Interestingly, expression of SeV C'-Flag was sufficient to promote hSpt16^{SUMO}
489 depletion in 293T cells in the absence of other SeV proteins. Moreover, this SeV C'-
490 mediated hSpt16^{SUMO} depletion was blocked in the presence of bortezomib (**Fig 7D**).
491 Interestingly, SeV C'-Flag could also deplete SUMOylated forms of the HA-hSpt16$^{\Delta NLS}$
492 mutant that cannot enter the nucleus (**Fig S6**). Importantly, SeV C'-Flag expression also
493 reduced SUMOylated Spt16 levels in mouse 3T3 cells (**Fig S7**), indicating that this viral
494 activity is retained in a natural SeV host species. These results collectively suggest that

495 like VSV M, SeV C' promotes proteasomal degradation of SUMOylated host Spt16
496 proteins in the cytoplasm.

497 We next examined if any of the shorter C proteins (C, Y1, and Y2) could also deplete
498 hSpt16^{SUMO} levels. Interestingly, only C' and C proteins were capable of depleting
499 hSpt16^{SUMO} in 293T cells (**Fig 7E**), suggesting the N-terminal 23 a.a. common between
500 C' and C proteins, but absent in Y1 and Y2 proteins (**Fig 7C**), are critical for targeting
501 hSpt16^{SUMO} for degradation. To determine if this 23 a.a. region was sufficient to promote
502 hSpt16^{SUMO} depletion, we fused these residues to the N-terminus of a GFP-Flag
503 construct, creating SeV C'$^{12\text{-}34}$-GFP-Flag. Strikingly, expression of SeV C'$^{12\text{-}34}$-GFP-Flag
504 was sufficient to deplete hSpt16^{SUMO} levels (**Fig 7F**).

505 Human parainfluenza virus-1 (HPIV-1), also known as human respirovirus 1, is a
506 clinically important paramyxovirus that is the leading cause of laryngotracheobronchitis
507 (croup) in children, a disease associated with swelling of the airways and difficulty
508 breathing [55]. HPIV-1 is closely related to SeV, sharing similar genetic and antigenic
509 properties. For example, the C proteins of SeV and HPIV-1 are ~70% identical [56].
510 Therefore, we examined the effect of hSpt16 RNAi on the replication of a GFP-encoding
511 HPIV-1 strain (HPIV-1-GFP) and the ability of this virus to target hSpt16^{SUMO} for
512 degradation. We found hSpt16 RNAi to enhance HPIV-1-GFP replication in human cells
513 (**Fig 7G**). Interestingly, as with SeV infection, hSpt16^{SUMO} was specifically depleted in
514 A549 cells by 24 hpi with HPIV-1-GFP (**Fig 7H).** Moreover, expression of a HPIV-1 C'-
515 Flag construct in 293T cells was sufficient to deplete hSpt16^{SUMO} and this depletion was
516 blocked by bortezomib (**Fig 7I**). Collectively, these results suggest that murine and
517 human paramyxovirus-encoded C proteins function as FEAR pathway antagonists that
518 target SUMOylated host Spt16 proteins for degradation.

519 **VSV M and paramyxovirus C proteins are structurally unrelated**

520

521 Given that both VSV M and paramyxovirus C proteins promote hSpt16^{SUMO} degradation,
522 we compared these proteins for similarity at primary (a.a. sequence) and tertiary
523 (structural) levels. Using basic local alignment search tool (BLAST) [57] we did not
524 observe any significant similarity between VSV M and either SeV C' or HPIV-1 C'
525 sequences.

526 We next examined tertiary structures of these proteins. Although a full-length VSV M
527 structure for the Indiana serotype used in our study has not been solved, the structure of
528 a VSV M fragment encompassing the globular domain (a.a. 44-229) (**Fig S8A**) bound to
529 Rae1-Nup98 complexes has been reported (4OWR) [58] (**Fig S8B**). In 4OWR, M
530 contacts Rae1-Nup98 complexes using three distinct regions that project from a "fist-
531 like" globular domain: a finger (a.a. 49-61), a thumb (a.a. 213-223), and a "web" region
532 (a.a. 142-144). Importantly, the finger motif, encompassing the M51 residue, makes
533 critical contacts with residues in a Rae1 β-propeller [58], illustrating the importance of
534 this region to host interactions. Since it was our goal to compare complete VSV M and
535 paramyxovirus C' protein structures to one another, we generated a full-length (a.a. 1-
536 229) VSV M structure using Alphafold2 [59](**Fig S8C**) and then compared this with
537 4OWR by overlaying them (**Fig S8D**) and conducting pairwise similarity tests using
538 RSCB PDB [60] to assign root mean square deviation (RMSD) values and template
539 modeling (TM) scores (**Fig S8E**). RMSD scores of <3 Å and TM scores >0.5 were
540 considered to have similar overall folds while those producing RMSD values >3 Å and
541 TM scores <0.5 were considered to be structurally unrelated [61]. Pairwise comparisons

542 between 4OWR and our predicted VSV M structure produced a RMSD of 1.82 Å and a
543 TM score of 0.93, providing confidence in our Alphafold2-generated VSV M structure.

544 We then used full-length SeV C' and HPIV-1 C' proteins (**Fig S9A**) to generate
545 structures with Alphafold2. We aligned our Alphafold2 SeV C' structure with a solved
546 structure from a SeV C fragment (a.a. 99-204) in complex with host Alix proteins (6KP3)
547 [62] (**Fig S9B-D**). Although 6KP3 is missing the N-terminal 23 a.a. region in SeV C' (a.a.
548 12-34) involved in hSpt16^{SUMO} depletion (**Fig S9A**), it contains most of the structured
549 globular domain (a.a. 88-215), allowing us to conduct a pairwise comparison to
550 determine how well the Alphafold2 structure aligned with 6KP3. We obtained a RSMD
551 value of 1.22 Å and TM score of 0.92 (**Fig S9E**), suggesting that the regions we could
552 compare were similar in structure, giving us confidence in the Alpahfold2 model.
553 Interestingly, the N-terminal domain of SeV C' (a.a. 1-87) in the Alphafold2 model is
554 completely unstructured with the exception of an alpha helix (a.a. 14-34) we term "α1"
555 that largely encompasses the region involved in hSpt16^{SUMO} depletion (a.a. 12-34) (**Fig**
556 **S9A and C**). Unfortunately, structures for HPIV-1 C proteins are not currently available,
557 therefore we used an Alphafold2 model of full-length HPIV-1 C' (**Fig S9F**) to overlay with
558 our predicted SeV C' structure (**Fig S9G**). Importantly, pairwise comparisons of these
559 SeV and HPIV-1 structures generated a RSMD of 2.57 Å and TM score of 0.66 (**Fig**
560 **S9H**), consistent with the high degree of conservation of these paramyxovirus proteins
561 [56]. Interestingly, we again found the N-terminal region (a.a. 1-93) of HPIV-1 C' to be
562 entirely disordered with the exception of a short alpha helix (a.a. 18-25, α1) that
563 corresponds to the N-terminal half of α1 in SeV C' (**Fig S9A and G**). These data suggest
564 that paramyxovirus C proteins have a conserved alpha helical structure that is likely
565 important for mediating hSpt16^{SUMO} depletion.

566 Finally, we overlaid our Alphafold2-generated models of full length VSV M and
567 paramyxoviruses C' proteins (**Fig S10A**) and used RMSD and TM analyses to compare
568 VSV M to either paramyxovirus protein. In both pairwise comparisons, we found VSV M
569 to exhibit RMSD values >3 Å and TM scores <0.5, indicating that these proteins are
570 structurally unrelated (**Fig S10B**). Collectively, these data suggest that VSV M and
571 paramyxovirus proteins are structurally unrelated, supporting the notion that
572 rhabdoviruses and paramyxoviruses evolved distinct factors to target hSpt16^{SUMO} for
573 degradation.

574 **Discussion**

575

576 The FEAR pathway was revealed by our discovery that poxvirus A51R proteins
577 antagonize this pathway [6], highlighting the fact that viral immune evasion factors can
578 provide insights into the critical host defenses that combat viral infection. While this
579 antiviral pathway was clearly important for combating DNA viruses, its relevance to RNA
580 viruses was less clear.

581

582 Here, we used VSV as a model RNA virus to examine if these viruses actively induce
583 and evade the FEAR pathway. We chose this virus in part because we previously
584 observed a measurable increase in VSV replication after hSpt16 depletion in human
585 cells [6], hinting at the possibility that this virus may be restricted by the FEAR pathway.
586 However, our discovery here that hSpt16 or ETS-1 depletion more strongly enhanced
587 the replication of VSV^{M51R} versus wild-type VSV, implicated the VSV M protein as a
588 suppressor of the FEAR pathway. Analysis of VSV-infected cell lysates led to our
589 unexpected discovery that, unlike VV A51R, which tethers hSpt16^{SUMO} to microtubules

590 [6], VSV M specifically promotes the proteasomal degradation of hSpt16^{SUMO} (**Fig 8**).
591 The inability of VSV^{M51R} strains to degrade hSpt16^{SUMO} explains the strong induction of
592 ETS-1 expression by these viruses. Importantly, the fact that VSV M expressed from a
593 plasmid could not only deplete hSpt16^{SUMO}, but also block ETS-1 induction by the ΔA51R
594 VV strain, indicates it can antagonize ETS-1 expression independently of other VSV
595 proteins. Moreover, our microscopy and cell fractionation studies suggest that wild-type,
596 but not M51R mutant, VSV M also prevents ETS-1 nuclear accumulation as a second
597 mechanism to inhibit the FEAR pathway.
598
599 The molecular mechanisms by which VSV M promotes hSpt16^{SUMO} degradation and
600 prevents ETS-1 nuclear accumulation are active areas of investigation. Given that the
601 most well-characterized defect of the M51R M mutant is its inability to interact with the
602 host Rae1-Nup98 mRNA export complex, we were surprised that Rae1 or Nup98
603 depletion had no effect on VSV-mediated hSpt16^{SUMO} depletion. Given that the M51
604 residue resides in a "finger-like" projection that protrudes from the globular domain of
605 VSV M [58], it may be a docking site for not only Rae1 but also for additional host
606 factors. We speculate that VSV M may use this finger projection to recruit ubiquitin-
607 proteasome system-related machinery (e.g. E3 ubiquitin ligases) that target hSpt16^{SUMO}
608 for degradation (**Fig 8**). Indeed, the repurposing of host E3 ligases to degrade antiviral
609 host factors has been widely observed among DNA and RNA viruses [63, 64]. Prior work
610 has shown that VSV M can inhibit nuclear translocation mediated by specific
611 karyopherin/importin protein family members in xenopus oocytes and this activity is lost
612 in the M51R mutant [65, 66]. Thus, it is possible that VSV M interferes with import
613 factors required for ETS-1 nuclear translocation.
614

615 Our discovery that VSV$^{\Delta M51}$/ VSV^{M51R} strains are defective in FEAR pathway antagonism
616 has led to important implications for their use in oncolytic virotherapy. A major drawback
617 of these strains is their inability to effectively replicate in cancer cell types that are still
618 capable of mounting effective antiviral responses [17, 40, 67]. Prior work had shown that
619 786-0 cells are highly refractory to VSV$^{\Delta M51}$ but that compounds termed "viral sensitizers"
620 that inhibit IFN responses can enhance the replication in, and killing of, these cells by
621 this oncolytic strain [18, 21, 68]. Our data demonstrating that hSpt16 RNAi enhances the
622 replication of a VSV$^{\Delta M51}$strain in these cells suggest that IFN-independent responses (i.e.
623 the FEAR pathway) are also relevant to the restriction of this strain. Moreover, we found
624 the FACT inhibitor, CBL0137, to be a promising viral sensitizer that improved VSV$^{\Delta M51}$
625 replication in these and other human cancer lines known to be resistant to infection by
626 VSV$^{\Delta M51}$/VSV^{M51R} oncolytic strains. Importantly, CBL0137 is already being pursued in
627 clinical trials as a cancer chemotherapeutic [33] as FACT upregulation is often observed
628 during oncogenesis and is associated with more aggressive cancers [31]. Such FACT
629 upregulation may also lead to more potent FACT-dependent antiviral responses,
630 potentially posing barriers to oncolytic virus replication in tumors. Thus, it will be
631 important to determine in future studies if combined (VSV$^{\Delta M51}$+CBL0137) treatment can
632 improve oncolytic virotherapy efficacy in animal models.
633
634 This study has also provided insight into the poorly understood abortive infection of VSV
635 in lepidopteran insect cells and the rescue of VSV replication in these cells by poxvirus
636 A51R proteins [9]. We previously found Spt16 proteins from various mammalian, insect,
637 and nematode cell lysates to exhibit the same, two-band pattern on IBs found in human
638 cell extracts, suggesting SUMOylation of Spt16 proteins is highly conserved among both
639 vertebrate and invertebrate eukaryotes [6]. More formal evidence for this was provided

640 here where we demonstrated that treatment with a SUMOylation inhibitor (tannic acid)
641 [47] could specifically eliminate the higher molecular weight form of LdSpt16 in *L. dispar*-
642 derived LD652 cells. Strikingly, despite being encoded by a mammalian poxvirus, VV
643 A51R was able to interact with LdSpt16^{SUMO}. This is likely due to the high degree of
644 conservation of the A51R-binding domain [6] among human and moth Spt16 proteins.
645 Our findings that: 1) VSV M cannot deplete LdSpt16^{SUMO} levels; 2) A51R proteins lacking
646 a functional Spt16-binding domain cannot rescue VSV replication in *L. dispar* cells; and
647 3) LdSpt16 RNAi rescues VSV replication, all strongly implicate LdSpt16^{SUMO} in VSV
648 host range restriction in these cells. Importantly, these results also suggest an ancient
649 role for SUMOylated Spt16 proteins in eukaryotic antiviral immunity. Future studies will
650 be needed to determine if insect ETS transcription factors [69] are also involved in virus
651 restriction and whether the FEAR pathway is indeed intact in invertebrates.
652
653 Investigation of paramyxovirus-FEAR pathway interactions revealed a remarkable
654 example of independent evolution of a common immune evasion mechanism by NNS
655 RNA viruses. Despite a lack of primary a.a. sequence or structural homology between
656 VSV M and paramyxovirus C proteins, they could both promote proteasome-dependent
657 degradation of hSpt16^{SUMO} (**Fig 8**). The specific targeting of SUMOylated Spt16 proteins
658 by pox-, rhabdo-, and paramyxoviruses suggests these host factors activate a critical
659 node of antiviral immunity. Interestingly, SeV and HPIV-1 C proteins have also been
660 shown to antagonize STAT protein function to inhibit IFN signaling [50, 51]. Thus, SeV
661 and HPIV-1 are likely under similar evolutionary pressure to inhibit key immune
662 responses pathway components such as STAT1 and Spt16^{SUMO} in their murine and
663 human hosts. Future studies will be aimed at determining if paramyxovirus C and VSV M
664 use a common or distinct host interactions to ultimately achieve hSpt16^{SUMO} degradation,

665 but our current work clearly defines these proteins as the first RNA virus-encoded FEAR
666 pathway antagonists.
667
668 In conclusion, our work has demonstrated that RNA viruses can activate and evade the
669 FEAR pathway, indicating this pathway is relevant to this important class of pathogens.
670 Major questions remain regarding how RNA viruses activate the FEAR pathway and how
671 ETS-1 activation eventually leads to virus restriction. Studies are ongoing to explore
672 these exciting areas of FEAR pathway biology. Moreover, whether other RNA virus
673 families antagonize the FEAR pathway is an active area of investigation. Ultimately, a
674 greater understanding of the activation and evasion of the FEAR pathway by viruses will
675 help us better appreciate the role of this host response in the evolutionary arms race
676 between viruses and their hosts.
677

678 **Materials and Methods**

679
680 Specific details regarding the source of all key experimental reagents (primers, plasmids,
681 Abs, viruses, cell lines, etc.) can be found in **Table S1**.
682
683 **Cell lines and primary cultures.** Mammalian cell lines were maintained at 37°C in 5%
684 CO_2 atmosphere. A549, U2OS, 293T, 786-0, NIH 3T3, Vero, and BHK-21 cells were
685 cultured in DMEM supplemented with 10% FBS. RPMI 7951 cells were cultured in
686 EMEM supplemented with 10% FBS. BSC-40 cells were passaged in MEM containing
687 5% FBS. All media above additionally contained 1% non-essential amino acids, 1% L-
688 glutamine, and 1% antibiotic/antimycotic (Gibco). LD652 were cultured in a 1:1 mixture

689 of Ex-Cell 420 (Sigma) and Graces insect medium (Invitrogen) supplemented with 10%
690 FBS at 27°C under normal atmospheric conditions [9, 70].
691
692 **Viruses and virus titrations**. VSV-GFP and VSV$^{\Delta M51}$-GFP strains were amplified in
693 either Vero or BHK-21 cells using low MOI infections [9, 71]. All other VSV strains were
694 amplified using low MOI infections in BHK-21 cells. SeV-GFP and HPIV-1-GFP stocks
695 were obtained from Viratree. BSC-40 cells were used for VV stock preparation [9].
696 Unless otherwise noted, virus strains were titrated by plaque assay (VSV-LUC,
697 ΔA51R^{FA51R}, ΔA51R) or fluorescent foci/plaque assay (VSV-eGFP, VSV^{M51R}-eGFP,
698 VSV$^{\Delta M51}$-GFP, SeV-GFP, HPIV-1-GFP) on BSC-40 cell monolayers, with a 1.5% low-
699 melting point agarose (Invitrogen) overlay used for VSV titrations [6]. In some cases,
700 VSV-GFP and VSV$^{\Delta M51}$-GFP stocks were titered on Vero cells [71]. Experimental viral
701 infections were incubated for 1 h in serum free DMEM at 37°C before the inoculum was
702 replaced with complete media for the remainder of the infection with the exception of
703 SeV-GFP and HPIV-1 cultures, which were kept in serum free DMEM containing either
704 1% TrypLE Select (Invitrogen) or 5 μg/ml acetylated trypsin (Sigma). Where indicated,
705 replacement media after 1 h of infection contained indicated doses of CBL0137 (Selleck
706 Chemicals) and was kept in the media until the end of the experiment. At indicated times
707 post-infection, infected cell culture supernatants were collected, clarified by
708 centrifugation, and clarified supernatant titers were determined by serial dilution followed
709 by plaque assay or fluorescent foci/plaque assay [6].
710
711 **Expression vectors.** The human ETS-1-HA pEZ-M07 expression vector was obtained
712 from GeneCopoeia. VSV M-Flag and M51R/ΔM51 mutant derivatives were constructed
713 by gene synthesis (Gene Universal) with inclusion of *Sac*II and *Pac*I sites for cloning into

714 *Sac*II/*Pac*I-digested pcDNA3 [6]. VSV M-Flag was also cloned into the insect p166
715 expression vector [9] using *Sac*II/*Pac*I sites. SeV C'-Flag and HPIV-1 C'-Flag expression
716 constructs were also generated using gene synthesis and cloned into pCNDA3 using
717 flanking *Sac*II/*Pac*I sites. SeV C-, Y1-, and Y2-Flag expression plasmids were
718 constructed from PCR amplification from the full-length SeV C' sequence. The SeV
719 C'$^{M12-R34}$-GFP-Flag pcDNA3 construct was made from PCR amplifying GFP-Flag from
720 pcDNA3 with a forward primer encoding the M12-R34 sequence. All SeV-related
721 constructs were cloned into pCDNA3 using flanking *Sac*II/*Pac*I sites. Wild-type VV Flag-
722 A51R and Flag-A51R$^{158-162Ala}$ open reading frames were cloned into the *Sac*II/*Pac*I sites
723 of p166 by *Sac*II/*Pac*I digest of Flag-A51R and Flag-A51R$^{158-162Ala}$ pcDNA3 vectors [6].
724 The HA-hSpt16 and HA-hSpt16$^{\Delta NLS}$ pEZ-M06 expression vectors have been described
725 [6]. The Flag-GFP pcDNA3 and p166 vectors have been described [6, 9]. All genes were
726 sequence verified. Expression plasmids were transfected into indicated mammalian cell
727 lines as previously described using Lipofectamine 2000 (Invitrogen) in Opti-MEM I
728 (Gibco) [9] overnight and then media was replaced with complete culture media.
729 Plasmids transfected into LD652 cells were used FuGENE HD (Promega) (LD652 cells)
730 [72]. Cells were for the indicated times prior to further processing [e.g. protein extraction
731 (see below)].
732
733 **General protein extraction and inhibitor treatments.** Cells were washed with
734 phosphate-buffered saline (PBS) prior to scraping and transfer into a 1.5 mL
735 microcentrifuge tube for centrifugation at 800 x *g* at 4°C for 15 min. Cell pellets were
736 resuspended in either 1x Reporter Lysis Buffer (Promega) containing cOmplete™
737 EDTA-free Protease Inhibitor Cocktail (Roche) and 1 mM phenylmethylsulfonyl fluoride
738 (PMSF) and freeze-thawed prior to addition of 5x SDS-PAGE loading buffer (100 mM tris

739 HCl, pH 6.8, 4% SDS, 12% (v/v) glycerol, 4 mM DTT, 0.02% (w/v) Bromophenol Blue) or
740 were resuspended in Pierce RIPA buffer (containing cOmplete™ EDTA-free Protease
741 Inhibitor Cocktail and 1 mM PMSF) prior to addition of 5x SDS-PAGE loading buffer.
742 Where indicated, cells were treated with 10 μM tannic acid for 4 h prior to protein
743 harvest. Also, where indicated, bortezomib (Selleck Chemicals) (25 nM), MG132
744 (Sigma) (40 μM), or DMSO (Corning) (vehicle control) was added to cells 6 h post-
745 transfection and was kept in media until protein extraction.
746
747 **Immunoblotting.** WCE were boiled for 10 min prior to SDS-PAGE electrophoresis at 50
748 V for approximately 4 h. Separated proteins were transferred in Towbin Buffer (BioRad)
749 onto nitrocellulose membranes at 150 mA at 4°C for 90 min and blocked with Odyssey
750 Blocking Buffer (LI-COR) for 1 h at RT. Membranes were blotted with primary Ab
751 overnight at 4°C, with actin serving as a loading control. After 3 x 5 min PBS-T (PBS,
752 0.1% Tween) washes, membranes were incubated in secondary Ab conjugated to an
753 IRDye (LI-COR) for 1 h, washed 3 x 5 min in PBS-T, then a final 5 min PBS wash.
754 Membranes were then imaged with an Odyssey Fc Imager (LI-COR).
755
756 **Immunoprecipitation.** Infection-based co-immunoprecipitation experiments were
757 performed as described with minor modifications [6]. Briefly, 10^6 LD652 cells were
758 seeded overnight, then infected with $\Delta A51R^{FA51R}$ (MOI=25) for 24 h. Prior to cell lysis,
759 cells were washed with equal volumes of PBS twice. Cells were lysed in IP lysis buffer
760 (cOmplete™ EDTA-free Protease Inhibitor Cocktail, 1 mM PMSF, 25 mM Tris-HCl at pH
761 7.4, 150 mM NaCl, 0.5% NP-40) and subjected to shearing and sonication (two-15
762 second sonications with a 30 second interval). Samples were benzonase (Sigma)
763 treated (250 units/mL) for 1 h at RT. 10% of "input" was collected, and remaining lysate

764 was end-over-end incubated with 5 µg of primary Ab overnight at 4°C (rabbit-anti-Flag or
765 isotype control Ab). Then, lysates were incubated with PureProteome protein A/G
766 magnetic beads (Sigma) for 1-2 h, extensively washed, and immunoprecipitants eluted
767 in 60 µl 2x SDS-PAGE loading buffer. IPs of total SUMOylated protein fractions in mock-
768 , VSV-eGFP, or VSV^{M51R}-eGFP-infected (MOI=10) A549 cells for 12 h used either
769 SUMO-1 or SUMO-2/3 Ab included with the Signal Seeker SUMOylation 1 or 2/3
770 Detection Kit (Cytoskeleton) and IPs were carried out according to the manufacturer
771 instructions [6].
772
773 **Cell fractionation.** Cell fractionation and subsequent densitometric analyses were
774 conducted as previously described [6]. Briefly, cells were infected at the indicated MOI
775 and times for the indicated times prior to fractionation using the Subcellular Protein
776 Fractionation Kit (Thermo Scientific) into either cytosolic or nuclear fractions.
777 Densitometry-based band quantifications were performed using ImageJ software (NIH,
778 version 1.51n). It is important to note that because the lysis buffer volume used in the
779 fractionation procedure is dependent upon the initial cell pellet size (which varied
780 between infection conditions), and the fractionation buffers were not compatible with
781 protein quantification assays, we only compared cytosolic versus nuclear distribution of a
782 particular protein within (and not between) each infection condition [6]. Quantification of
783 the percentage of total cellular ETS-1 protein present in the nuclear fraction within each
784 indicated infection condition was calculated by dividing the nuclear fraction ETS-1 band
785 densitometric values by the sum of total (cytosolic +nuclear) ETS- 1 densitometric
786 values.
787

788 **RNAi in cell culture.** All siRNAs were obtained from Sigma's pre-designed siRNA
789 library (see **Table S1)**. The hSpt16 and ETS-1-targeted siRNAs have been previously
790 validated [6]. Transient siRNA-mediated knockdown was achieved by reverse
791 transfecting mammalian cells with Lipofectamine 2000 according to manufacturer's
792 protocol for 48-72 h prior to viral infection [6]. RNAi knockdowns in LD652 cells were
793 performed as previously described using *in vitro*-transcribed dsRNAs transfected with
794 Cellfectin II (Invitrogen) in Sf-900 II serum free medium [9]. Transfection medium was
795 replaced with complete culture medium after overnight culture. Sequences of primers
796 used to generate dsRNA targeting GFP (control) or *LdSpt16* gene sequences are
797 in **Table S1**.
798
799 **Luciferase assays.** Luciferase assays in LD652 WCE were performed as previously
800 described with minor modifications [9, 72]. Briefly, at the indicated times post-infection,
801 cells were washed in PBS, collected by centrifugation (2000 rpm, 10 min, 4°C) and lysed
802 in reporter lysis buffer (Promega). Lysates were spotted to 96-well dishes, mixed with
803 Luciferase Assay Reagent (Promega) and arbitrary light units (LU) were measured using
804 an FLUOstar Omega Plate reader (BMG Labtech).
805
806 **Antibodies.** Information regarding antibodies used in this study, including their source,
807 is available in **Table S1**.
808
809 **Fluorescence microscopy and cell viability assays.** At indicated times post-infection,
810 cells were stained with 200 µL of serum free media containing NucBlue (Thermo Fisher)
811 for 30 min followed by replacement with 1 mL of PBS. Cells were imaged using a 4X
812 objective on an EVOS-FL fluorescence microscope (Thermo Fisher) using DAPI and

813 GFP cubes. Each condition had three replicate wells, and at least four images/well were
814 collected for analysis. Image analysis was conducted using Fiji (NIH) to quantify the
815 normalized GFP signal/field by dividing total GFP signal by total DAPI (NucBlue) signals.
816 Positive signal was determined by using uninfected wells lacking NucBlue stain to set a
817 minimum threshold in both DAPI and GFP channels that was applied to the remaining
818 dataset. Fold change in GFP signals were calculated by dividing normalized GFP values
819 of experimental treatments with normalized GFP values in control treatments (indicated
820 in each figure). For GFP foci imaging and cell viability analysis of 786-0 cells infected
821 with VSV$^{\Delta M51}$-GFP, cells were grown to confluency in multi-well dishes, infected with
822 VSV$^{\Delta M51}$-GFP at the indicated MOIs and treated with 0.3-3μM CBL0137 (or media
823 alone) 1 hpi using the Agilent Bravo liquid handling system (Agilent, CA, USA). 24 hpi,
824 GFP images were captured by fluorescence microscopy using an ArrayScan Thermo
825 Scientific Cellomics) and GFP foci were quantified. Cell viability was assessed 48
826 hpi using resazurin sodium salt (Sigma-Aldrich) after a 2.5 h incubation using a BioTek
827 Microplate Reader (BioTek Instruments Inc.).
828
829 **Immunofluorescence microscopy.** For staining cells under mock, VSV-eGFP, or
830 VSV^{M51R}-eGFP infection conditions, cells were seeded at a density of 30,000 cells per
831 coverslip, cultured overnight, then infected (MOI=10) for 12 hpi. Cells were fixed with 4%
832 paraformaldehyde (Sigma), incubated with blocking buffer (PBS with 1% BSA and 0.1%
833 Triton-X) for 1 h, stained with mouse anti-ETS-1 Ab for 2 h, washed extensively with
834 blocking buffer, incubated with Alexa Fluor-conjugated secondary Ab for 1h, and then
835 again washed extensively. Coverslips were then mounted onto glass slides using
836 ProLong™ Diamond anti-fade with DAPI (Thermo Scientific) and imaged with an
837 Olympus FV10i confocal laser scanning microscope (version 2.1) equipped with

838 Olympus Fluoview software (version 4.2a). Images were deconvoluted with CellSens
839 Imaging software (version 1.18). Similar imaging methods were used for U2OS cells
840 transiently transfected with VSV M-Flag, VSV M^{M51R}-Flag and ETS-1-HA expression
841 plasmids, except rabbit anti-Flag and mouse anti-HA primary Ab were used for staining.
842
843 **Protein sequence alignment and structure prediction**

844 Sequences of VSV M (NCBI accession: 7UMK_B), SeV C' (P04862.3), and HPIV-1 C'
845 (NP_604434.1) were predicted using AlphaFoldv2 [59] and analyzed using PyMOL **(**The
846 PyMOL Molecular Graphics System version 1.2r3pre, Schrödinger, LLC**.).** To determine
847 structural similarity between VSV M, SeV C' and HPIV-1 C', pairwise structural
848 alignments were conducted using RSCB PDB [60] to assign RMSD and TM scores.
849 RMSD values of <3 Å and TM scores >0.5 were considered to have similar overall fold,
850 while pairwise comparisons producing RMSD values >3 Å and TM scores <0.5 were
851 considered to be structurally unrelated [61].
852
853 **Statistical analyses.** All statistical analyses were conducted using GraphPad Prism
854 (version 8.0) software and *P* values <0.05 were considered statistically significant.
855 Sample sizes, statistical tests used, and *P* value information are indicated in the
856 respective figure or figure legend for each quantitative experiment.
857

858 ## Data Availability

859
860 The authors declare that the main data supporting the findings of this study are available
861 within the article and/or Supplementary Information. Source data will be provided after

initial peer review as per the editor's instructions as Supplementary Information files due to the size and time required to prepare.

Author Contributions

Conceptualization, E.A., R.A., J.S.D., and D.B.G.; Methodology, E.A., R.A., J.S.D., and D.B.G.; Investigation, E.A., D.S., A.E., R.A., M.M.S., and D.B.G.; Data Curation, E.A., D.S, A.E., R.A., M.M.S., and D.B.G.; Writing—original draft, E.A. and D.B.G.; Writing—Review & Editing, E.A., D.S., A.E., R.A., M.M.S., J.S.D., and D.B.G.; Visualization, E.A., A.E., R.A., and D.B.G. Supervision, D.B.G., R.A., and J.S.D.; Funding Acquisition, J.S.D and D.B.G.

Competing Interest Statement

The authors declare no competing interests. The funders had no role in the design of the study; in the collection, analyses, or interpretation of data; in the writing of the manuscript; or in the decision to publish the results.

Acknowledgments

We thank members of the Gammon lab for helpful discussion regarding the manuscript. We also thank Dr. Beatriz Fontoura (UTSW Medical Center) for advice regarding the manuscript.

887 **References**
888

889 1. Tenthorey JL, Emerman M, Malik HS. Evolutionary Landscapes of Host-Virus Arms
890 Races. Annu Rev Immunol. 2022;40:271-94. Epub 2022/01/27. doi: 10.1146/annurev-immunol-
891 072621-084422. PubMed PMID: 35080919.
892 2. Chan YK, Gack MU. Viral evasion of intracellular DNA and RNA sensing. Nat Rev
893 Microbiol. 2016;14(6):360-73. Epub 2016/05/14. doi: 10.1038/nrmicro.2016.45. PubMed PMID:
894 27174148; PubMed Central PMCID: PMCPMC5072394.
895 3. Zhu J, Chiang C, Gack MU. Viral evasion of the interferon response at a glance. J Cell
896 Sci. 2023;136(12). Epub 2023/06/21. doi: 10.1242/jcs.260682. PubMed PMID: 37341132;
897 PubMed Central PMCID: PMCPMC10411950.
898 4. Nan Y, Nan G, Zhang YJ. Interferon induction by RNA viruses and antagonism by viral
899 pathogens. Viruses. 2014;6(12):4999-5027. Epub 2014/12/17. doi: 10.3390/v6124999. PubMed
900 PMID: 25514371; PubMed Central PMCID: PMCPMC4276940.
901 5. Beachboard DC, Horner SM. Innate immune evasion strategies of DNA and RNA viruses.
902 Curr Opin Microbiol. 2016;32:113-9. Epub 2016/06/12. doi: 10.1016/j.mib.2016.05.015. PubMed
903 PMID: 27288760; PubMed Central PMCID: PMCPMC4983539.
904 6. Rex EA, Seo D, Chappidi S, Pinkham C, Brito Oliveira S, Embry A, et al. FEAR antiviral
905 response pathway is independent of interferons and countered by poxvirus proteins. Nat
906 Microbiol. 2024;9(4):988-1006. Epub 2024/03/28. doi: 10.1038/s41564-024-01646-5. PubMed
907 PMID: 38538832.
908 7. Winkler DD, Luger K. The histone chaperone FACT: structural insights and mechanisms
909 for nucleosome reorganization. J Biol Chem. 2011;286(21):18369-74. Epub 2011/04/02. doi:
910 10.1074/jbc.R110.180778. PubMed PMID: 21454601; PubMed Central PMCID:
911 PMCPMC3099653.
912 8. Duina AA. Histone Chaperones Spt6 and FACT: Similarities and Differences in Modes of
913 Action at Transcribed Genes. Genet Res Int. 2011;2011:625210. Epub 2011/01/01. doi:
914 10.4061/2011/625210. PubMed PMID: 22567361; PubMed Central PMCID: PMCPMC3335715.
915 9. Gammon DB, Duraffour S, Rozelle DK, Hehnly H, Sharma R, Sparks ME, et al. A single
916 vertebrate DNA virus protein disarms invertebrate immunity to RNA virus infection. Elife. 2014;3.
917 Epub 2014/06/27. doi: 10.7554/eLife.02910. PubMed PMID: 24966209; PubMed Central PMCID:
918 PMCPMC4112549.
919 10. Liu G, Cao W, Salawudeen A, Zhu W, Emeterio K, Safronetz D, et al. Vesicular
920 Stomatitis Virus: From Agricultural Pathogen to Vaccine Vector. Pathogens. 2021;10(9). Epub
921 2021/09/29. doi: 10.3390/pathogens10091092. PubMed PMID: 34578125; PubMed Central
922 PMCID: PMCPMC8470541.
923 11. Lawson ND, Stillman EA, Whitt MA, Rose JK. Recombinant vesicular stomatitis viruses
924 from DNA. Proc Natl Acad Sci U S A. 1995;92(10):4477-81. Epub 1995/05/09. doi:
925 10.1073/pnas.92.10.4477. PubMed PMID: 7753828; PubMed Central PMCID: PMCPMC41967.
926 12. Whelan SP, Ball LA, Barr JN, Wertz GT. Efficient recovery of infectious vesicular
927 stomatitis virus entirely from cDNA clones. Proc Natl Acad Sci U S A. 1995;92(18):8388-92. Epub
928 1995/08/29. doi: 10.1073/pnas.92.18.8388. PubMed PMID: 7667300; PubMed Central PMCID:
929 PMCPMC41162.
930 13. Abdelmageed AA, Ferran MC. The Propagation, Quantification, and Storage of Vesicular
931 Stomatitis Virus. Curr Protoc Microbiol. 2020;58(1):e110. Epub 2020/08/25. doi:
932 10.1002/cpmc.110. PubMed PMID: 32833351; PubMed Central PMCID: PMCPMC7449588.
933 14. Suder E, Furuyama W, Feldmann H, Marzi A, de Wit E. The vesicular stomatitis virus-
934 based Ebola virus vaccine: From concept to clinical trials. Hum Vaccin Immunother.
935 2018;14(9):2107-13. Epub 2018/05/15. doi: 10.1080/21645515.2018.1473698. PubMed PMID:
936 29757706; PubMed Central PMCID: PMCPMC6183239.
937 15. Case JB, Rothlauf PW, Chen RE, Kafai NM, Fox JM, Smith BK, et al. Replication-
938 Competent Vesicular Stomatitis Virus Vaccine Vector Protects against SARS-CoV-2-Mediated
939 Pathogenesis in Mice. Cell Host Microbe. 2020;28(3):465-74 e4. Epub 2020/08/18. doi:

940 10.1016/j.chom.2020.07.018. PubMed PMID: 32798445; PubMed Central PMCID:
941 PMCPMC7391951.
942 16. Holbrook MC, Goad DW, Grdzelishvili VZ. Expanding the Spectrum of Pancreatic
943 Cancers Responsive to Vesicular Stomatitis Virus-Based Oncolytic Virotherapy: Challenges and
944 Solutions. Cancers (Basel). 2021;13(5). Epub 2021/04/04. doi: 10.3390/cancers13051171.
945 PubMed PMID: 33803211; PubMed Central PMCID: PMCPMC7963195.
946 17. Felt SA, Grdzelishvili VZ. Recent advances in vesicular stomatitis virus-based oncolytic
947 virotherapy: a 5-year update. J Gen Virol. 2017;98(12):2895-911. Epub 2017/11/17. doi:
948 10.1099/jgv.0.000980. PubMed PMID: 29143726; PubMed Central PMCID: PMCPMC5845697.
949 18. Selman M, Ou P, Rousso C, Bergeron A, Krishnan R, Pikor L, et al. Dimethyl fumarate
950 potentiates oncolytic virotherapy through NF-kappaB inhibition. Sci Transl Med. 2018;10(425).
951 Epub 2018/01/26. doi: 10.1126/scitranslmed.aao1613. PubMed PMID: 29367345.
952 19. Stojdl DF, Lichty BD, tenOever BR, Paterson JM, Power AT, Knowles S, et al. VSV
953 strains with defects in their ability to shutdown innate immunity are potent systemic anti-cancer
954 agents. Cancer Cell. 2003;4(4):263-75. Epub 2003/10/31. doi: 10.1016/s1535-6108(03)00241-1.
955 PubMed PMID: 14585354.
956 20. Le Boeuf F, Diallo JS, McCart JA, Thorne S, Falls T, Stanford M, et al. Synergistic
957 interaction between oncolytic viruses augments tumor killing. Mol Ther. 2010;18(5):888-95. Epub
958 2010/03/18. doi: 10.1038/mt.2010.44. PubMed PMID: 20234341; PubMed Central PMCID:
959 PMCPMC2890112.
960 21. Arulanandam R, Batenchuk C, Varette O, Zakaria C, Garcia V, Forbes NE, et al.
961 Microtubule disruption synergizes with oncolytic virotherapy by inhibiting interferon translation and
962 potentiating bystander killing. Nat Commun. 2015;6:6410. Epub 2015/03/31. doi:
963 10.1038/ncomms7410. PubMed PMID: 25817275.
964 22. Alluqmani N, Jirovec A, Taha Z, Varette O, Chen A, Serrano D, et al. Vanadyl sulfate-
965 enhanced oncolytic virus immunotherapy mediates the antitumor immune response by
966 upregulating the secretion of pro-inflammatory cytokines and chemokines. Front Immunol.
967 2022;13:1032356. Epub 2022/12/20. doi: 10.3389/fimmu.2022.1032356. PubMed PMID:
968 36532027; PubMed Central PMCID: PMCPMC9749062.
969 23. Blackham AU, Northrup SA, Willingham M, D'Agostino RB, Jr., Lyles DS, Stewart JHt.
970 Variation in susceptibility of human malignant melanomas to oncolytic vesicular stomatitis virus.
971 Surgery. 2013;153(3):333-43. Epub 2012/10/30. doi: 10.1016/j.surg.2012.09.003. PubMed PMID:
972 23102637; PubMed Central PMCID: PMCPMC3561511.
973 24. Rajani KR, Pettit Kneller EL, McKenzie MO, Horita DA, Chou JW, Lyles DS. Complexes
974 of vesicular stomatitis virus matrix protein with host Rae1 and Nup98 involved in inhibition of host
975 transcription. PLoS Pathog. 2012;8(9):e1002929. Epub 2012/10/03. doi:
976 10.1371/journal.ppat.1002929. PubMed PMID: 23028327; PubMed Central PMCID:
977 PMCPMC3460625.
978 25. Faria PA, Chakraborty P, Levay A, Barber GN, Ezelle HJ, Enninga J, et al. VSV disrupts
979 the Rae1/mrnp41 mRNA nuclear export pathway. Mol Cell. 2005;17(1):93-102. Epub 2005/01/05.
980 doi: 10.1016/j.molcel.2004.11.023. PubMed PMID: 15629720.
981 26. Bishnoi S, Tiwari R, Gupta S, Byrareddy SN, Nayak D. Oncotargeting by Vesicular
982 Stomatitis Virus (VSV): Advances in Cancer Therapy. Viruses. 2018;10(2). Epub 2018/02/24. doi:
983 10.3390/v10020090. PubMed PMID: 29473868; PubMed Central PMCID: PMCPMC5850397.
984 27. Fenton SE, Saleiro D, Platanias LC. Type I and II Interferons in the Anti-Tumor Immune
985 Response. Cancers (Basel). 2021;13(5). Epub 2021/04/04. doi: 10.3390/cancers13051037.
986 PubMed PMID: 33801234; PubMed Central PMCID: PMCPMC7957896.
987 28. Kottke T, Tonne J, Evgin L, Driscoll CB, van Vloten J, Jennings VA, et al. Oncolytic
988 virotherapy induced CSDE1 neo-antigenesis restricts VSV replication but can be targeted by
989 immunotherapy. Nat Commun. 2021;12(1):1930. Epub 2021/03/28. doi: 10.1038/s41467-021-
990 22115-1. PubMed PMID: 33772027; PubMed Central PMCID: PMCPMC7997928.
991 29. Nguyen TL, Abdelbary H, Arguello M, Breitbach C, Leveille S, Diallo JS, et al. Chemical
992 targeting of the innate antiviral response by histone deacetylase inhibitors renders refractory
993 cancers sensitive to viral oncolysis. Proc Natl Acad Sci U S A. 2008;105(39):14981-6. Epub

994 2008/09/26. doi: 10.1073/pnas.0803988105. PubMed PMID: 18815361; PubMed Central PMCID:
995 PMCPMC2567479.
996 30. Oda N, Abe M, Sato Y. ETS-1 converts endothelial cells to the angiogenic phenotype by
997 inducing the expression of matrix metalloproteinases and integrin beta3. J Cell Physiol.
998 1999;178(2):121-32. Epub 1999/02/27. doi: 10.1002/(SICI)1097-4652(199902)178:2<121::AID-
999 JCP1>3.0.CO;2-F. PubMed PMID: 10048576.
1000 31. Garcia H, Miecznikowski JC, Safina A, Commane M, Ruusulehto A, Kilpinen S, et al.
1001 Facilitates chromatin transcription complex is an "accelerator" of tumor transformation and
1002 potential marker and target of aggressive cancers. Cell Rep. 2013;4(1):159-73. Epub 2013/07/09.
1003 doi: 10.1016/j.celrep.2013.06.013. PubMed PMID: 23831030; PubMed Central PMCID:
1004 PMCPMC5886782.
1005 32. Dittmer J. The role of the transcription factor Ets1 in carcinoma. Semin Cancer Biol.
1006 2015;35:20-38. Epub 2015/09/24. doi: 10.1016/j.semcancer.2015.09.010. PubMed PMID:
1007 26392377.
1008 33. Gasparian AV, Burkhart CA, Purmal AA, Brodsky L, Pal M, Saranadasa M, et al.
1009 Curaxins: anticancer compounds that simultaneously suppress NF-kappaB and activate p53 by
1010 targeting FACT. Sci Transl Med. 2011;3(95):95ra74. Epub 2011/08/13. doi:
1011 10.1126/scitranslmed.3002530. PubMed PMID: 21832239; PubMed Central PMCID:
1012 PMCPMC6281439.
1013 34. Park YH, Jung HH, Ahn JS, Im YH. Ets-1 upregulates HER2-induced MMP-1 expression
1014 in breast cancer cells. Biochem Biophys Res Commun. 2008;377(2):389-94. Epub 2008/10/15.
1015 doi: 10.1016/j.bbrc.2008.09.135. PubMed PMID: 18851945.
1016 35. Whitlow ZW, Connor JH, Lyles DS. New mRNAs are preferentially translated during
1017 vesicular stomatitis virus infection. J Virol. 2008;82(5):2286-94. Epub 2007/12/21. doi:
1018 10.1128/JVI.01761-07. PubMed PMID: 18094194; PubMed Central PMCID: PMCPMC2258916.
1019 36. Kato H, Sato S, Yoneyama M, Yamamoto M, Uematsu S, Matsui K, et al. Cell type-
1020 specific involvement of RIG-I in antiviral response. Immunity. 2005;23(1):19-28. Epub 2005/07/26.
1021 doi: 10.1016/j.immuni.2005.04.010. PubMed PMID: 16039576.
1022 37. Yu H, Bruneau RC, Brennan G, Rothenburg S. Battle Royale: Innate Recognition of
1023 Poxviruses and Viral Immune Evasion. Biomedicines. 2021;9(7). Epub 2021/08/07. doi:
1024 10.3390/biomedicines9070765. PubMed PMID: 34356829; PubMed Central PMCID:
1025 PMCPMC8301327.
1026 38. Schoggins JW. Interferon-Stimulated Genes: What Do They All Do? Annu Rev Virol.
1027 2019;6(1):567-84. Epub 2019/07/10. doi: 10.1146/annurev-virology-092818-015756. PubMed
1028 PMID: 31283436.
1029 39. Mahajan R, Delphin C, Guan T, Gerace L, Melchior F. A small ubiquitin-related
1030 polypeptide involved in targeting RanGAP1 to nuclear pore complex protein RanBP2. Cell.
1031 1997;88(1):97-107. Epub 1997/01/10. doi: 10.1016/s0092-8674(00)81862-0. PubMed PMID:
1032 9019411.
1033 40. Boulukos KE, Pognonec P, Rabault B, Begue A, Ghysdael J. Definition of an Ets1 protein
1034 domain required for nuclear localization in cells and DNA-binding activity in vitro. Mol Cell Biol.
1035 1989;9(12):5718-21. Epub 1989/12/01. doi: 10.1128/mcb.9.12.5718-5721.1989. PubMed PMID:
1036 2555704; PubMed Central PMCID: PMCPMC363744.
1037 41. Lulli V, Romania P, Morsilli O, Gabbianelli M, Pagliuca A, Mazzeo S, et al.
1038 Overexpression of Ets-1 in human hematopoietic progenitor cells blocks erythroid and promotes
1039 megakaryocytic differentiation. Cell Death Differ. 2006;13(7):1064-74. Epub 2005/11/19. doi:
1040 10.1038/sj.cdd.4401811. PubMed PMID: 16294212.
1041 42. Fleyshman D, Prendergast L, Safina A, Paszkiewicz G, Commane M, Morgan K, et al.
1042 Level of FACT defines the transcriptional landscape and aggressive phenotype of breast cancer
1043 cells. Oncotarget. 2017;8(13):20525-42. Epub 2017/04/21. doi: 10.18632/oncotarget.15656.
1044 PubMed PMID: 28423528; PubMed Central PMCID: PMCPMC5400524.
1045 43. Kim M, Neznanov N, Wilfong CD, Fleyshman DI, Purmal AA, Haderski G, et al.
1046 Preclinical Validation of a Single-Treatment Infusion Modality That Can Eradicate Extremity

1047 Melanomas. Cancer Res. 2016;76(22):6620-30. Epub 2016/11/05. doi: 10.1158/0008-5472.CAN-
1048 15-2764. PubMed PMID: 27680682; PubMed Central PMCID: PMCPMC5609527.
1049 44. Dermawan JK, Hitomi M, Silver DJ, Wu Q, Sandlesh P, Sloan AE, et al. Pharmacological
1050 Targeting of the Histone Chaperone Complex FACT Preferentially Eliminates Glioblastoma Stem
1051 Cells and Prolongs Survival in Preclinical Models. Cancer Res. 2016;76(8):2432-42. Epub
1052 2016/02/28. doi: 10.1158/0008-5472.CAN-15-2162. PubMed PMID: 26921329; PubMed Central
1053 PMCID: PMCPMC4873320.
1054 45. Burkhart C, Fleyshman D, Kohrn R, Commane M, Garrigan J, Kurbatov V, et al. Curaxin
1055 CBL0137 eradicates drug resistant cancer stem cells and potentiates efficacy of gemcitabine in
1056 preclinical models of pancreatic cancer. Oncotarget. 2014;5(22):11038-53. Epub 2014/11/18. doi:
1057 10.18632/oncotarget.2701. PubMed PMID: 25402820; PubMed Central PMCID:
1058 PMCPMC4294371.
1059 46. Zhang J, Cong Q, Rex EA, Hallwachs W, Janzen DH, Grishin NV, et al. Gypsy moth
1060 genome provides insights into flight capability and virus-host interactions. Proc Natl Acad Sci U S
1061 A. 2019;116(5):1669-78. Epub 2019/01/16. doi: 10.1073/pnas.1818283116. PubMed PMID:
1062 30642971; PubMed Central PMCID: PMCPMC6358702.
1063 47. Suzawa M, Miranda DA, Ramos KA, Ang KK, Faivre EJ, Wilson CG, et al. A gene-
1064 expression screen identifies a non-toxic sumoylation inhibitor that mimics SUMO-less human
1065 LRH-1 in liver. Elife. 2015;4. Epub 2015/12/15. doi: 10.7554/eLife.09003. PubMed PMID:
1066 26653140; PubMed Central PMCID: PMCPMC4749390.
1067 48. Cureton DK, Massol RH, Saffarian S, Kirchhausen TL, Whelan SP. Vesicular stomatitis
1068 virus enters cells through vesicles incompletely coated with clathrin that depend upon actin for
1069 internalization. PLoS Pathog. 2009;5(4):e1000394. Epub 2009/04/25. doi:
1070 10.1371/journal.ppat.1000394. PubMed PMID: 19390604; PubMed Central PMCID:
1071 PMCPMC2667253.
1072 49. Mohd-Qawiem F, Nawal-Amani AR, Faranieyza-Afiqah F, Yasmin AR, Arshad SS,
1073 Norfitriah MS, et al. Paramyxoviruses in rodents: A review. Open Vet J. 2022;12(6):868-76. Epub
1074 2023/01/19. doi: 10.5455/OVJ.2022.v12.i6.14. PubMed PMID: 36650879; PubMed Central
1075 PMCID: PMCPMC9805762.
1076 50. Wang C, Wang T, Duan L, Chen H, Hu R, Wang X, et al. Evasion of Host Antiviral Innate
1077 Immunity by Paramyxovirus Accessory Proteins. Front Microbiol. 2021;12:790191. Epub
1078 2022/02/18. doi: 10.3389/fmicb.2021.790191. PubMed PMID: 35173691; PubMed Central
1079 PMCID: PMCPMC8841848.
1080 51. Pisanelli G, Pagnini U, Iovane G, Garcia-Sastre A. Type I and Type II Interferon
1081 Antagonism Strategies Used by Paramyxoviridae: Previous and New Discoveries, in Comparison.
1082 Viruses. 2022;14(5). Epub 2022/05/29. doi: 10.3390/v14051107. PubMed PMID: 35632848;
1083 PubMed Central PMCID: PMCPMC9145045.
1084 52. Morita N, Tanaka Y, Takeuchi K, Kitagawa Y, Sakuma R, Koide N, et al. SeV C Protein
1085 Plays a Role in Restricting Macrophage Phagocytosis by Limiting the Generation of Intracellular
1086 Double-Stranded RNA. Front Microbiol. 2022;13:780534. Epub 2022/03/11. doi:
1087 10.3389/fmicb.2022.780534. PubMed PMID: 35265056; PubMed Central PMCID:
1088 PMCPMC8899396.
1089 53. Garcin D, Latorre P, Kolakofsky D. Sendai virus C proteins counteract the interferon-
1090 mediated induction of an antiviral state. J Virol. 1999;73(8):6559-65. Epub 1999/07/10. doi:
1091 10.1128/JVI.73.8.6559-6565.1999. PubMed PMID: 10400752; PubMed Central PMCID:
1092 PMCPMC112739.
1093 54. Grogan CC, Moyer SA. Sendai virus wild-type and mutant C proteins show a direct
1094 correlation between L polymerase binding and inhibition of viral RNA synthesis. Virology.
1095 2001;288(1):96-108. Epub 2001/09/07. doi: 10.1006/viro.2001.1068. PubMed PMID: 11543662.
1096 55. Marcink TC, Englund JA, Moscona A. Paramyxoviruses: Parainfluenza Viruses. In:
1097 Kaslow RA, Stanberry LR, Powers AM, editors. Viral Infections of Humans: Epidemiology and
1098 Control. New York, NY: Springer US; 2020. p. 1-50.
1099 56. Lo MK, Sogaard TM, Karlin DG. Evolution and structural organization of the C proteins of
1100 paramyxovirinae. PLoS One. 2014;9(2):e90003. Epub 2014/03/04. doi:

1101 10.1371/journal.pone.0090003. PubMed PMID: 24587180; PubMed Central PMCID:
1102 PMCPMC3934983.
1103 57. Altschul SF, Gish W, Miller W, Myers EW, Lipman DJ. Basic local alignment search tool.
1104 J Mol Biol. 1990;215(3):403-10. Epub 1990/10/05. doi: 10.1016/S0022-2836(05)80360-2.
1105 PubMed PMID: 2231712.
1106 58. Quan B, Seo HS, Blobel G, Ren Y. Vesiculoviral matrix (M) protein occupies nucleic acid
1107 binding site at nucleoporin pair (Rae1 * Nup98). Proc Natl Acad Sci U S A. 2014;111(25):9127-
1108 32. Epub 2014/06/14. doi: 10.1073/pnas.1409076111. PubMed PMID: 24927547; PubMed
1109 Central PMCID: PMCPMC4078809.
1110 59. Jumper J, Evans R, Pritzel A, Green T, Figurnov M, Ronneberger O, et al. Highly
1111 accurate protein structure prediction with AlphaFold. Nature. 2021;596(7873):583-9. Epub
1112 2021/07/16. doi: 10.1038/s41586-021-03819-2. PubMed PMID: 34265844; PubMed Central
1113 PMCID: PMCPMC8371605 have filed non-provisional patent applications 16/701,070 and
1114 PCT/EP2020/084238, and provisional patent applications 63/107,362, 63/118,917, 63/118,918,
1115 63/118,921 and 63/118,919, each in the name of DeepMind Technologies Limited, each pending,
1116 relating to machine learning for predicting protein structures. The other authors declare no
1117 competing interests.
1118 60. Bittrich S, Segura J, Duarte JM, Burley SK, Rose Y. RCSB protein Data Bank: exploring
1119 protein 3D similarities via comprehensive structural alignments. Bioinformatics. 2024;40(6). Epub
1120 2024/06/13. doi: 10.1093/bioinformatics/btae370. PubMed PMID: 38870521; PubMed Central
1121 PMCID: PMCPMC11212067.
1122 61. Xu J, Zhang Y. How significant is a protein structure similarity with TM-score = 0.5?
1123 Bioinformatics. 2010;26(7):889-95. Epub 2010/02/19. doi: 10.1093/bioinformatics/btq066.
1124 PubMed PMID: 20164152; PubMed Central PMCID: PMCPMC2913670.
1125 62. Oda K, Matoba Y, Sugiyama M, Sakaguchi T. Structural Insight into the Interaction of
1126 Sendai Virus C Protein with Alix To Stimulate Viral Budding. J Virol. 2021;95(19):e0081521. Epub
1127 2021/07/22. doi: 10.1128/JVI.00815-21. PubMed PMID: 34287046; PubMed Central PMCID:
1128 PMCPMC8428403.
1129 63. Mahon C, Krogan NJ, Craik CS, Pick E. Cullin E3 ligases and their rewiring by viral
1130 factors. Biomolecules. 2014;4(4):897-930. Epub 2014/10/15. doi: 10.3390/biom4040897. PubMed
1131 PMID: 25314029; PubMed Central PMCID: PMCPMC4279162.
1132 64. Loboda AP, Soond SM, Piacentini M, Barlev NA. Lysine-specific post-translational
1133 modifications of proteins in the life cycle of viruses. Cell Cycle. 2019;18(17):1995-2005. Epub
1134 2019/07/12. doi: 10.1080/15384101.2019.1639305. PubMed PMID: 31291816; PubMed Central
1135 PMCID: PMCPMC6681785.
1136 65. Her LS, Lund E, Dahlberg JE. Inhibition of Ran guanosine triphosphatase-dependent
1137 nuclear transport by the matrix protein of vesicular stomatitis virus. Science.
1138 1997;276(5320):1845-8. Epub 1997/06/20. doi: 10.1126/science.276.5320.1845. PubMed PMID:
1139 9188527.
1140 66. Petersen JM, Her LS, Varvel V, Lund E, Dahlberg JE. The matrix protein of vesicular
1141 stomatitis virus inhibits nucleocytoplasmic transport when it is in the nucleus and associated with
1142 nuclear pore complexes. Mol Cell Biol. 2000;20(22):8590-601. Epub 2000/10/25. doi:
1143 10.1128/MCB.20.22.8590-8601.2000. PubMed PMID: 11046154; PubMed Central PMCID:
1144 PMCPMC102164.
1145 67. Dittmer J. The biology of the Ets1 proto-oncogene. Mol Cancer. 2003;2:29. Epub
1146 2003/09/16. doi: 10.1186/1476-4598-2-29. PubMed PMID: 12971829; PubMed Central PMCID:
1147 PMCPMC194255.
1148 68. Phan M, Watson MF, Alain T, Diallo JS. Oncolytic Viruses on Drugs: Achieving Higher
1149 Therapeutic Efficacy. ACS Infect Dis. 2018;4(10):1448-67. Epub 2018/08/29. doi:
1150 10.1021/acsinfecdis.8b00144. PubMed PMID: 30152676.
1151 69. Garrett-Sinha LA. Review of Ets1 structure, function, and roles in immunity. Cell Mol Life
1152 Sci. 2013;70(18):3375-90. Epub 2013/01/05. doi: 10.1007/s00018-012-1243-7. PubMed PMID:
1153 23288305; PubMed Central PMCID: PMCPMC3636162.

1154 70. Winkler DD, Muthurajan UM, Hieb AR, Luger K. Histone chaperone FACT coordinates
1155 nucleosome interaction through multiple synergistic binding events. J Biol Chem.
1156 2011;286(48):41883-92. Epub 2011/10/05. doi: 10.1074/jbc.M111.301465. PubMed PMID:
1157 21969370; PubMed Central PMCID: PMCPMC3308894.
1158 71. Diallo JS, Vaha-Koskela M, Le Boeuf F, Bell J. Propagation, purification, and in vivo
1159 testing of oncolytic vesicular stomatitis virus strains. Methods Mol Biol. 2012;797:127-40. Epub
1160 2011/09/29. doi: 10.1007/978-1-61779-340-0_10. PubMed PMID: 21948474.
1161 72. Embry A, Baggett NS, Heisler DB, White A, de Jong MF, Kocsis BL, et al. Exploiting
1162 bacterial effector proteins to uncover evolutionarily conserved antiviral host machinery. PLoS
1163 Pathog. 2024;20(5):e1012010. Epub 2024/05/16. doi: 10.1371/journal.ppat.1012010. PubMed
1164 PMID: 38753575; PubMed Central PMCID: PMCPMC11098378.
1165 73. Wu W, Zhang W, Duggan ES, Booth JL, Zou MH, Metcalf JP. RIG-I and TLR3 are both
1166 required for maximum interferon induction by influenza virus in human lung alveolar epithelial
1167 cells. Virology. 2015;482:181-8. Epub 2015/04/17. doi: 10.1016/j.virol.2015.03.048. PubMed
1168 PMID: 25880109; PubMed Central PMCID: PMCPMC4461467.
1169 74. Loo YM, Fornek J, Crochet N, Bajwa G, Perwitasari O, Martinez-Sobrido L, et al. Distinct
1170 RIG-I and MDA5 signaling by RNA viruses in innate immunity. J Virol. 2008;82(1):335-45. Epub
1171 2007/10/19. doi: 10.1128/JVI.01080-07. PubMed PMID: 17942531; PubMed Central PMCID:
1172 PMCPMC2224404.

1173

1174 **Main Figure Legends**

1175

1176 **Fig 1. The FEAR pathway contributes to VSV restriction in human cells and is**
1177 **strongly activated by VSV^{M51R}-eGFP.** (A-B) VSV-eGFP (WT) and VSV^{M51R}-eGFP
1178 (M51R) titers 24 h post-infection (hpi) (MOI=0.001) in A549 cells transfected with
1179 indicated RNAi treatments using two independent siRNAs for either hSpt16 (A) or ETS-1
1180 (B) knockdown. Scram., scrambled siRNA. Data are means ± SD; n=3. Statistical
1181 significance in A and B were determined by unpaired two-tailed Student's t-tests
1182 between indicated treatments. * = P< 0.05; ** = P< 0.01; ns = not significant. (C)
1183 Immunoblot (IB) of endogenous ETS-1 in A549 whole cell extract (WCE) after infection
1184 with VSV-eGFP (WT) or VSV^{M51R}-eGFP (M51R) (MOI=10). (D) Densitometric
1185 quantification of ETS-1 from multiple IB experiments as in C. Data are means ± SD; n=3.
1186 Results of unpaired two-tailed Student's t-test between ETS-1 levels in mock WCE and
1187 infected WCE are shown above each bar graph as: * = P< 0.05, ** = P< 0.01, or ns = not
1188 significant. (E) IB of U2OS cell WCE transfected with empty vector (EV) or ETS-1-HA
1189 constructs 48 h post-transfection. (F) Representative fluorescence microscopy images of

1190 U2OS cells transfected as in E and then infected with VSV-eGFP for 16 h. NucBlue was
1191 used to mark cell nuclei and to account for cell number. Scale bar = 500 μm. (G)
1192 Quantification of total GFP signal/field normalized to NucBlue signal for experiments
1193 from F. Data are means ± SD; n=3. Statistical significance was determined by unpaired
1194 two-tailed Student's t-test between indicated treatments. ** = P< 0.01.
1195
1196 **Fig 2. VSV, but not VSV^{M51R}, promotes hSpt16^{SUMO} depletion to prevent ETS-1**
1197 **induction.** (A) IB of FACT subunit levels in WCE from A549 cells infected with VSV-
1198 eGFP (WT) or VSV^{M51R}-eGFP (M51R) for indicated hpi (MOI=10). (B-D) Densitometric
1199 quantification of IB experiments in A for hSpt16^{SUMO} (B) SUMOless hSpt16 (C) or SSRP1
1200 levels (D). Data are means ± SD; n=3. In B-D, results of unpaired two-tailed Student's t-
1201 test between protein levels in mock WCE and infected WCE are shown above each bar
1202 graph as: * = P< 0.05, ** = P< 0.01, or ns = not significant. (E-F) IB of
1203 immunoprecipitated SUMO-1- (E) or SUMO-2/3- (F) conjugated protein fractions in WCE
1204 from mock-, VSV-eGFP -, or VSV^{M51R}-eGFP-infected A549 cells (MOI=3) 18 hpi. Cont.,
1205 control IP. RanGAP1 is a known SUMOylated protein and used as a control for
1206 enrichment of SUMOylated fractions [39]. GFP is a marker for infection. (G) IB of
1207 endogenous ETS-1 and hSpt16 levels and in WCE of scrambled- or hSpt16-siRNA-
1208 treated A549 cells 8 hpi with indicated strains (MOI=10).
1209
1210 **Fig 3. VSV M is sufficient to promote proteasomal degradation of cytoplasmic**
1211 **hSpt16^{SUMO} and to block ETS-1 expression.** (A) IB of endogenous hSpt16 in 293T
1212 WCE transfected with indicated Flag-tagged VSV protein expression constructs for 24 h.
1213 Empty vector, EV. Asterisks indicate probable VSV M degradation products. (B) IB of
1214 endogenous hSpt16 in 293T WCE transfected with indicated VSV M expression

1215 constructs 24 h post-transfection. EV and Flag-GFP constructs were negative controls.
1216 Asterisks indicate probable VSV M degradation products. (C) Immunofluorescence (IF)
1217 images of U2OS cells transfected with indicated HA-tagged hSpt16 constructs for 24 h.
1218 Scale bar = 5 μm. (D) IB of 293T WCE 24 h post-transfection with indicated HA-tagged
1219 hSpt16 constructs along with either EV, VSV M-Flag (WT), or VSV M^{M51R}-Flag (M51R)
1220 pcDNA3 vectors. Asterisks indicate probable VSV M degradation products. (E-F) 293T
1221 WCE transfected with indicated VSV M expression constructs in the absence or
1222 presence of bortezomib (E) or MG132 (F) proteasome inhibitor treatment. Vehicle
1223 (DMSO) treatments served as negative controls. Asterisks indicate probable VSV M
1224 degradation products. (G) IB of endogenous ETS-1 in U2OS WCE after transfection with
1225 indicated expression constructs for 24 h and then infected with VSV^{M51R}-eGFP (MOI
1226 =10) for 8 h. (H) Densitometric quantification of IB experiments in G. Data are means ±
1227 SD; n=3. (I) IB of endogenous ETS-1 in U2OS WCE after transfection with indicated
1228 expression constructs for 24 h and then infected with ΔA51R VV strain (MOI =10) for 8h.
1229 (J) Densitometric quantification of IB experiments in I. Data are means ± SD; n=4.
1230 Statistical significance in H and J were determined by unpaired two-tailed Student's t-
1231 tests between indicated treatments. ** = P< 0.01; ns = not significant.
1232
1233 **Fig 4. VSV M inhibits ETS-1 nuclear accumulation.** (A) IF staining of ETS-1 in mock-,
1234 VSV-eGFP (WT)-, or VSV^{M51R}-eGFP (M51R)-infected A549 cells 12 hpi (MOI=10). (B) IB
1235 of A549 cytoplasmic (C) and nuclear (N) fractions 12 hpi with indicated strains (MOI=10).
1236 Vimentin marks cytosolic fractions while histone H4 marks nuclear fractions [6]. (C)
1237 Densitometric quantification of multiple IB experiments as in B expressed as percentage
1238 of total (cytosolic+nuclear fractions) ETS-1 protein present in nuclear fractions. Data are
1239 means ± SD; n=3. Statistical significance was determined by unpaired two-tailed

1240 Student's t-test between indicated treatments. ** = P< 0.01. (D) IF staining of ETS-1 in
1241 mock-, VSV-eGFP-, or VSV^{M51R}-eGFP-infected U2OS cells 12 hpi (MOI=10). (E) IF
1242 staining of U2OS cells 24 h post co-transfection with ETS-1-HA expression vectors and
1243 either EV, VSV M-Flag, or VSV M^{M51R}-Flag expression vectors. Scale bars in A, D, and E
1244 = 5 μm.
1245
1246 **Fig 5. Suppression of FEAR pathway activation promotes oncolytic VSV strain**
1247 **replication in refractory cancer cell lines.** (A) VSV$^{\Delta M51}$-GFP titers 24 hpi (MOI=0.01) in
1248 786-0 cells transfected with indicated RNAi treatments. Data are means ± SD; n=3. (B)
1249 IB of 786-0 WCE from experiments in A at 24 hpi. (C) Representative fluorescence
1250 microscopy images 24 hpi with VSV$^{\Delta M51}$-GFP (MOI=0.05) in 786-0 cells in the presence
1251 of indicated doses of CBL0137. (D) Quantification of GFP foci 24 hpi (green line, read on
1252 right y-axis) after VSV$^{\Delta M51}$-GFP infection of 786-0 cells in the absence or presence of
1253 indicated doses of CBL0137. Cell viability 48 h post-treatment (read on left y-axis) of
1254 cultures containing only CBL0137 (blue line) or CBL0137+ VSV$^{\Delta M51}$-GFP (red line) is
1255 also shown. Data are means ± SD; n=3. (E) Titer of VSV$^{\Delta M51}$-GFP-infected 786-0 cells
1256 24 hpi (MOI=0.01) in the presence of indicated doses of CBL0137. Data are means ±
1257 SD; n=3. (F) IB of 786-0 WCE from experiments in E at 24 hpi. (G) Titer of VSV$^{\Delta M51}$-
1258 GFP-infected RPMI 7951 cells 24 hpi (MOI=0.01) in the presence of indicated doses of
1259 CBL0137. Data are means ± SD; n=3. Statistical significance in A, E, G, and H were
1260 determined by unpaired two-tailed Student's t-test between indicated treatments. * = P<
1261 0.05; ** = P< 0.01; ns, not significant.
1262

1263 **Fig 6. Abortive VSV replication in *L. dispar* cells can by complemented by VV**
1264 **A51R expression or by Spt16 RNAi.** (A) IB of *L. dispar* Spt16 (LdSpt16) in LD652
1265 WCE in the absence or presence of tannic acid (TA) treatment. (B) Co-IP of endogenous
1266 LdSpt16 with FA51R in ΔA51R^{FA51R}-infected (MOI=25) LD652 WCE. (C) Fold-change in
1267 luciferase (LUC) signal in LD652 cells transfected with indicated FA51R expression
1268 constructs for 24 h and then infected with VSV-LUC (MOI=10) for 48 h. Fold-change in
1269 LUC is plotted as relative to LUC signal in Flag-GFP (FGFP) transfection treatments
1270 (negative control). Data are means ± SD; n=3. (D) VSV-LUC titers from supernatants
1271 collected from C. Data are means ± SD; n=3. (E) Fold-change in LUC signal after 72 h of
1272 transfection with dsRNAs (for RNAi) targeting either GFP (control) or LdSpt16 (Spt16-
1273 A/B) and infection with VSV-LUC (MOI=10) for 48 h. Data are means ± SD; n=4. (F)
1274 VSV-LUC titers from supernatants collected from E. Data are means ± SD; n=4. (G) IB
1275 of LdSpt16 levels in LD652 WCE 48 h post-transfection with empty vector (EV) or
1276 increasing amounts of VSV M-Flag p166 expression vector. Statistical significance in C,
1277 D, E, and F were determined by unpaired two-tailed Student's t-test between indicated
1278 treatments. ** = P< 0.01; ns, not significant.
1279
1280 **Fig 7. Murine and human paramyxovirus-encoded C proteins also promote**
1281 **proteasome-dependent degradation of hSpt16^{SUMO}.** (A) SeV-GFP titers 48 hpi
1282 (MOI=0.01) in A549 cells after indicated RNAi treatments. Data are means ± SD; n=3.
1283 (B) IB of FACT subunit levels in mock- or SeV-GFP-infected (MOI=1) A549 WCE at
1284 indicated hpi. GFP is a marker of infection. (C) Schematic illustrating the four accessory
1285 SeV "C" proteins (C'1, C, Y1, and Y2) and their relative translation initiation sites (nts) in
1286 the SeV *P* transcript and resulting protein sizes (a.a.). Image modified from [54]. (D) IB

1287 of endogenous hSpt16 in 293T WCE transfected with indicated expression constructs for
1288 24 h in the absence or presence of bortezomib treatment. Asterisks indicates SeV C'-
1289 Flag degradation product. (E) IB of endogenous hSpt16 in 293T WCE transfected with
1290 indicated expression constructs for 24 h. Asterisks indicates SeV C'/C-Flag degradation
1291 products. (F) IB of endogenous hSpt16 in 293T WCE transfected with indicated
1292 expression constructs for 24 h. (G) HPIV-1-GFP titers 48 hpi (MOI=0.01) in A549 cells
1293 after indicated RNAi treatments. Data are means ± SD; n=3. (H) IB of FACT subunit
1294 levels in mock- or HPIV1-GFP-infected (MOI=1) A549 WCE at indicated hpi. GFP is a
1295 marker of infection. (I) IB of endogenous hSpt16 in 293T WCE transfected with indicated
1296 expression constructs for 24 h in the absence or presence of bortezomib treatment.
1297 Statistical significance in A and G were determined by unpaired two-tailed Student's t-
1298 test between indicated treatments. * = P< 0.05; ** = P< 0.01; ns, not significant.
1299
1300 **Fig 8. Model for DNA and RNA virus-encoded mechanisms to antagonize the**
1301 **FEAR pathway.** Poxvirus A51R proteins tether hSpt16^{SUMO} subunits to microtubules to
1302 prevent FACT complex formation and activation of ETS-1 expression in the nucleus. In
1303 contrast, VSV M and paramyxovirus (SeV, HPIV-1) C proteins promote degradation of
1304 hSpt16^{SUMO} subunits in the proteasome to block ETS-1 expression. This degradation-
1305 based mechanism may involve recruitment of host E3 ubiquitin ligases to target
1306 hSpt16^{SUMO} for degradation. VSV M may also inhibit FEAR pathway activation by
1307 impeding ETS-1 nuclear accumulation (not shown). Model for FEAR pathway is adapted
1308 from [6] and was created using Biorender.com.
1309
1310
1311 **Supplementary Figure Legends**

1312

1313 **Fig S1. VSV-induced ETS-1 expression is independent of RIG-I or IFN signaling.**
1314 (A, B) Representative IB (A) and quantification (B) of ETS-1 expression using IB of WCE
1315 from control or RIG-I knockout (KO) A549 cells infected with the indicated strains
1316 (MOI=10) for 8 h. Note: RIG-I is expressed at a low level in uninfected cells and is known
1317 to be induced by viral infection [73, 74], consistent with our results. (C, D)
1318 Representative IB (C) and quantification (D) of ETS-1 expression using IB of WCE from
1319 control or IRF3 KO A549 cells infected with the indicated strains (MOI=10) for 8 h. (E, F)
1320 Representative IB (E) and quantification (F) of ETS-1 expression using IB of WCE from
1321 control or STAT1 KO A549 cells infected with the indicated strains (MOI=10) for 8 h.
1322 Data in B, D, and F are means ± SD for n=3 experiments. Statistical significance in B, E,
1323 and F were determined by unpaired two-tailed Student's t-test between indicated
1324 treatments. For brevity, only the most relevant statistical comparisons are shown. * = P<
1325 0.05; ** = P< 0.01; ns, not significant.

1326

1327 **Fig S2. The VSV^{M51R}-eGFP strain is unable to deplete hSpt16^{SUMO} regardless of**
1328 **MOI.** IB of endogenous hSpt16 in A549 WCE after infection with VSV-eGFP or VSV^{M51R}-
1329 eGFP at the indicated MOI. GFP is used as a marker for infection.

1330

1331 **Fig S3. A VSV$^{\Delta M51}$ strain is unable to deplete hSpt16^{SUMO}.** IB of endogenous hSpt16 in
1332 A549 WCE after infection with VSV-GFP (WT) or VSV$^{\Delta M51}$-GFP (ΔM51) (MOI=3). GFP is
1333 used as a marker for infection.

1334

1335 **Fig S4. VSV M-mediated depletion of hSpt16^{SUMO} is independent of Rae1 and**
1336 **Nup98.** IB of endogenous hSpt16 in A549 whole cell extract (WCE) 72 h after RNAi of

1337 Rae1 (A) or Nup98 (B) under mock- or VSV-eGFP-infection (MOI = 10) conditions for 12
1338 h. VSV N and GFP are markers for infection. Scram., scrambled.
1339
1340 **Fig S5. Human and *Lymantria dispar*-encoded Spt16 proteins share a similar**
1341 **A51R-binding domain.** Alignment of the VV A51R-binding domain of hSpt16 [6]
1342 (accession: NP_009123.1) with corresponding region in LdSpt16 (accession:
1343 GCA_004115105.1). The overall amino acid identity of these regions is 72.8%.
1344 Alignment was made using NCBI Blast2p Software.
1345
1346 **Fig S6. SeV C' promotes depletion of SUMOylated Spt16 subunits present in the**
1347 **cytosol**. IB of HA-hSpt16 or HA-hSpt16$^{\Delta NLS}$ in 293T WCE 24 h after transfection with
1348 empty vector (EV) and or SeV C'-Flag expression constructs.
1349
1350 **Fig S7. SeV C' promotes depletion of SUMOylated Spt16 subunits in mouse 3T3**
1351 **cells.** IB of endogenous mouse Spt16 in 3T3 WCE 24 h after transfection with empty
1352 vector (EV) and or SeV C'-Flag expression constructs.
1353
1354 **Fig S8. VSV M protein structural modeling.** (A) VSV M protein map showing region
1355 surrounding M51 residue (red). NTE = N-terminal extension. Protein map based on
1356 reference [58]. B) 4OWR structure of VSV M fragment (a.a. 44-229) bound to Rae1-
1357 Nup98 complex [58]. (C) Alphafold2-generated structure of full-length (a.a. 1-229) VSV
1358 M (strain Indiana). (D) Overlay of structures from B and C. E) Results of pairwise
1359 comparison of structures in B and C showing RMSD (in Å) and TM values.
1360

1361 **Fig S9. Paramyxovirus C protein structural modeling.** (A) Protein maps of SeV C'
1362 and HPIV-1 C' showing region in SeV C' N-terminus sufficient for hSpt16^{SUMO}
1363 degradation (a.a. 12-34) aligned with corresponding region in HPIV-1 C'. NTE = N-
1364 terminal extension. Residues predicted to form alpha helical structures in the NTE are in
1365 red and purple for SeV C' and HPIV-1 C', respectively. (B) 6KP3 structure of SeV C'
1366 fragment (a.a. 99-204) bound to cellular Alix protein [62]. (C) Alphafold2-generated
1367 structure of full-length (a.a. 1-215) SeV C'. (D) Overlay of structures from B and C. (E)
1368 Results of pairwise comparison of structures in B and C showing RMSD (in Å) and TM
1369 values. (F) Alphafold2-generated structure of full-length (a.a. 1-219) HPIV-1 C'. (G)
1370 Overlay of structures from C and F. (H) Results of pairwise comparison of structures in B
1371 and C showing RMSD (in Å) and TM values.
1372
1373 **Fig S10. Structural comparison of VSV M to paramyxovirus C proteins.** (A) Overlay
1374 of Alphafold2-generated VSV M (Fig S8C), SeV C' (Fig S9C), and HPIV-1 C' (Fig S9F)
1375 structures. (B) Results of pairwise comparison of VSV M to either SeV C' or HPIV-1 C'
1376 structures showing RMSD (in Å) and TM values.
1377
1378 **Supplementary Tables**
1379
1380 **Table S1. Key Experimental Reagents.**

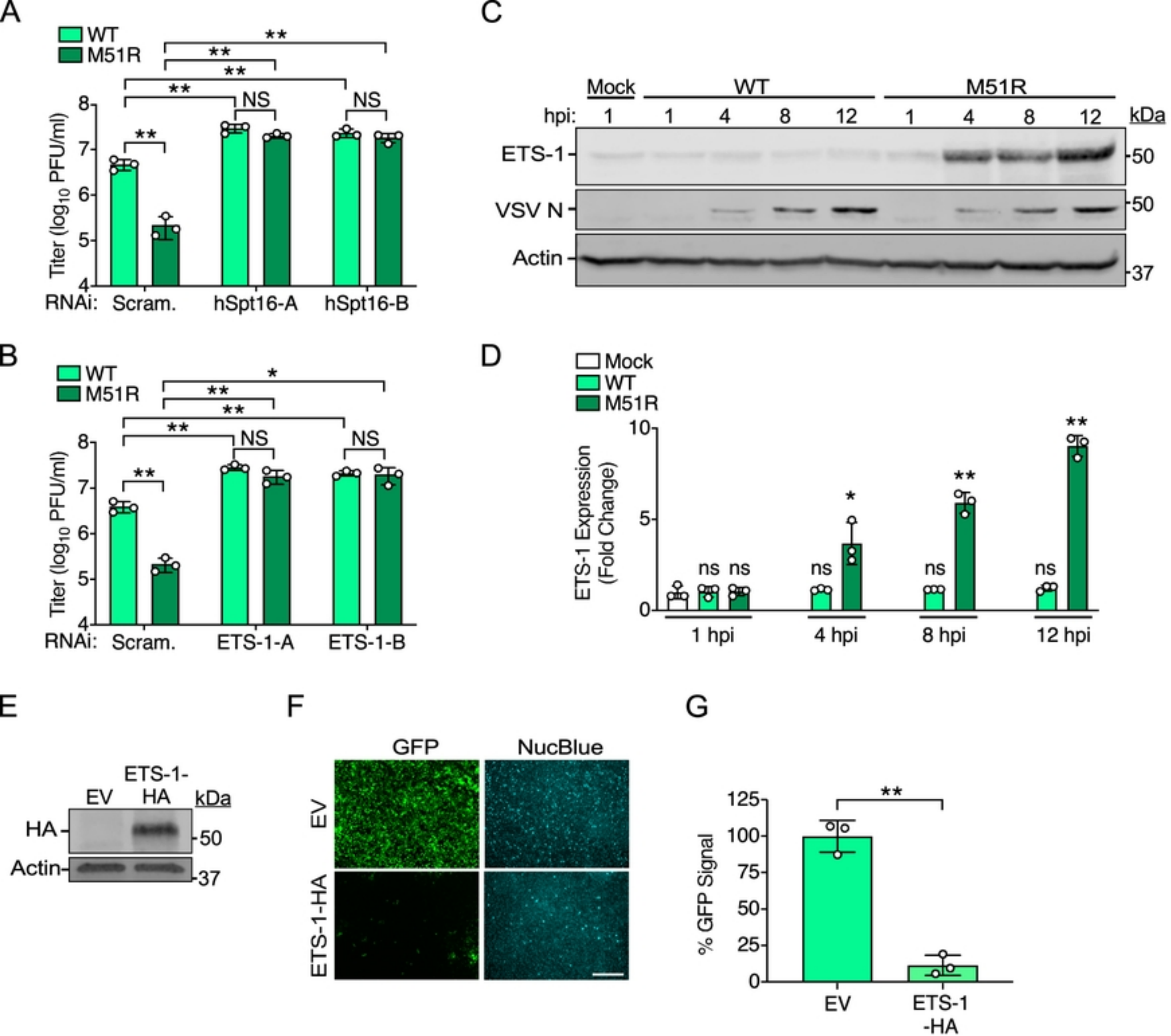
A
WT
M51R
Titer (log10 PFU/ml)
RNAi: Scram. hSpt16-A hSpt16-B
NS
B
RNAi: Scram. ETS-1-A ETS-1-B
C
Mock
WT
M51R
hpi: 1 1 4 8 12 1 4 8 12
kDa
ETS-1
VSV N
Actin
50
37
D
Mock
WT
M51R
ETS-1 Expression (Fold Change)
1 hpi
4 hpi
8 hpi
12 hpi
E
EV
ETS-1-HA
kDa
HA
Actin
F
GFP
NucBlue
EV
ETS-1-HA
G
% GFP Signal
EV
ETS-1 -HA

Figure 1

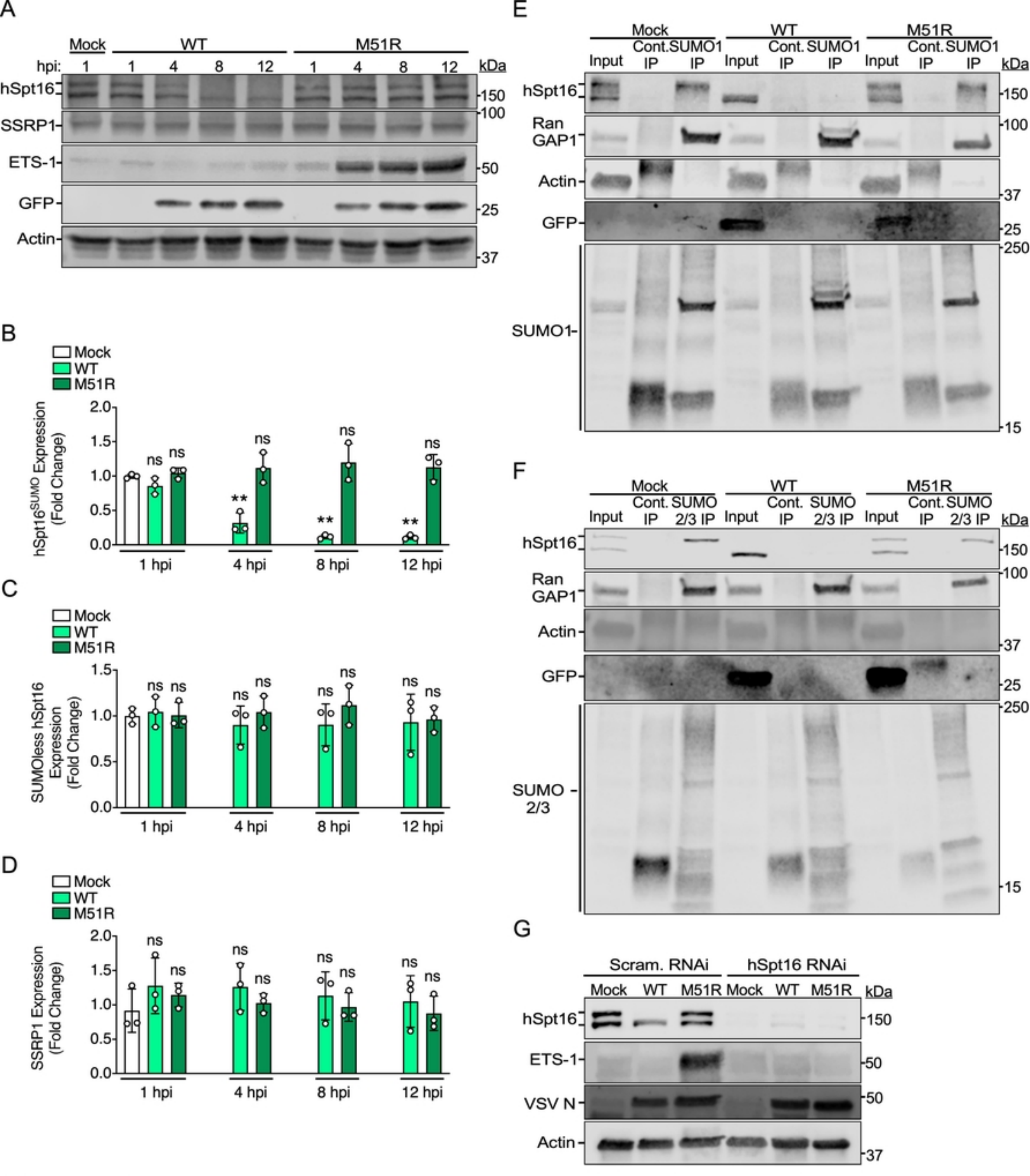
A
Mock
WT
M51R
hpi: 1 1 4 8 12 1 4 8 12
kDa
hSpt16
SSRP1
ETS-1
GFP
Actin
150
100
50
25
37
B
Mock
WT
M51R
hSpt16SUMO Expression (Fold Change)
2.0
1.5
1.0
0.5
0.0
ns
**
1 hpi
4 hpi
8 hpi
12 hpi
C
Mock
WT
M51R
SUMOless hSpt16 Expression (Fold Change)
1.5
1.0
0.5
0.0
ns
1 hpi
4 hpi
8 hpi
12 hpi
D
Mock
WT
M51R
SSRP1 Expression (Fold Change)
2.0
1.5
1.0
0.5
0.0
ns
1 hpi
4 hpi
8 hpi
12 hpi
E
Mock
WT
M51R
Input
Cont. IP
SUMO1 IP
kDa
hSpt16
Ran GAP1
Actin
GFP
SUMO1
150
100
37
25
250
15
F
Mock
WT
M51R
Input
Cont. IP
SUMO 2/3 IP
kDa
hSpt16
Ran GAP1
Actin
GFP
SUMO 2/3
150
100
37
25
250
15
G
Scram. RNAi
hSpt16 RNAi
Mock
WT
M51R
Mock
WT
M51R
kDa
hSpt16
ETS-1
VSV N
Actin
150
50
50
37

Figure 2

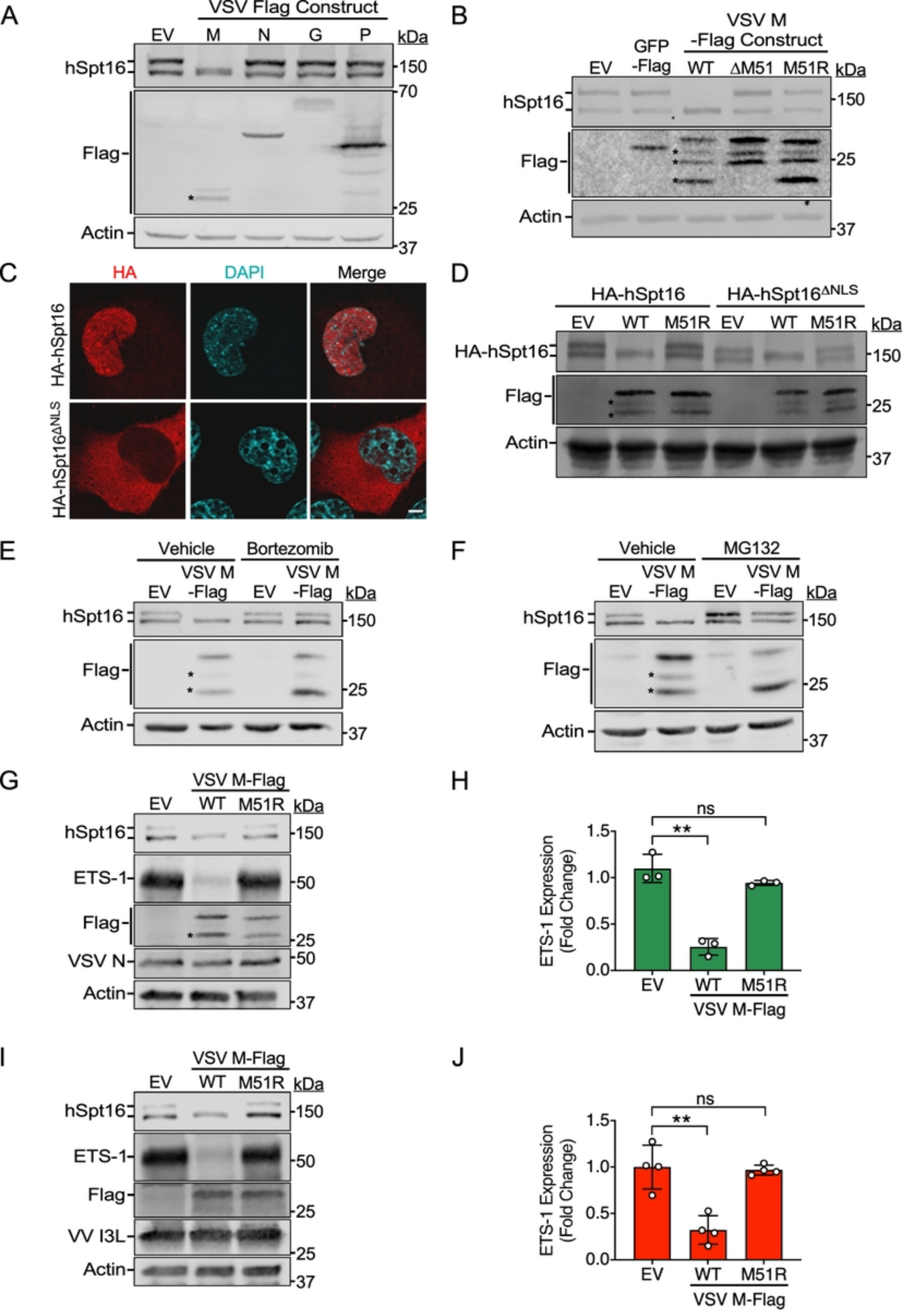
A
VSV Flag Construct
EV
M
N
G
P
kDa
hSpt16
150
70
Flag
25
Actin
37
B
VSV M
-Flag Construct
EV
GFP
-Flag
WT
ΔM51
M51R
kDa
hSpt16
150
Flag
25
Actin
37
C
HA
DAPI
Merge
HA-hSpt16
HA-hSpt16ΔNLS
D
HA-hSpt16
HA-hSpt16ΔNLS
EV
WT
M51R
EV
WT
M51R
kDa
HA-hSpt16
150
Flag
25
Actin
37
E
Vehicle
Bortezomib
VSV M
-Flag
EV
-Flag
EV
kDa
hSpt16
150
Flag
25
Actin
37
F
Vehicle
MG132
VSV M
-Flag
EV
-Flag
EV
kDa
hSpt16
150
Flag
25
Actin
37
G
VSV M-Flag
EV
WT
M51R
kDa
hSpt16
150
ETS-1
50
Flag
25
VSV N
50
Actin
37
H
ns
**
1.5
1.0
0.5
0.0
ETS-1 Expression
(Fold Change)
EV
WT
M51R
VSV M-Flag
I
VSV M-Flag
EV
WT
M51R
kDa
hSpt16
150
ETS-1
50
Flag
25
VV I3L
25
Actin
37
J
ns
**
1.5
1.0
0.5
0.0
ETS-1 Expression
(Fold Change)
EV
WT
M51R
VSV M-Flag

Figure 3

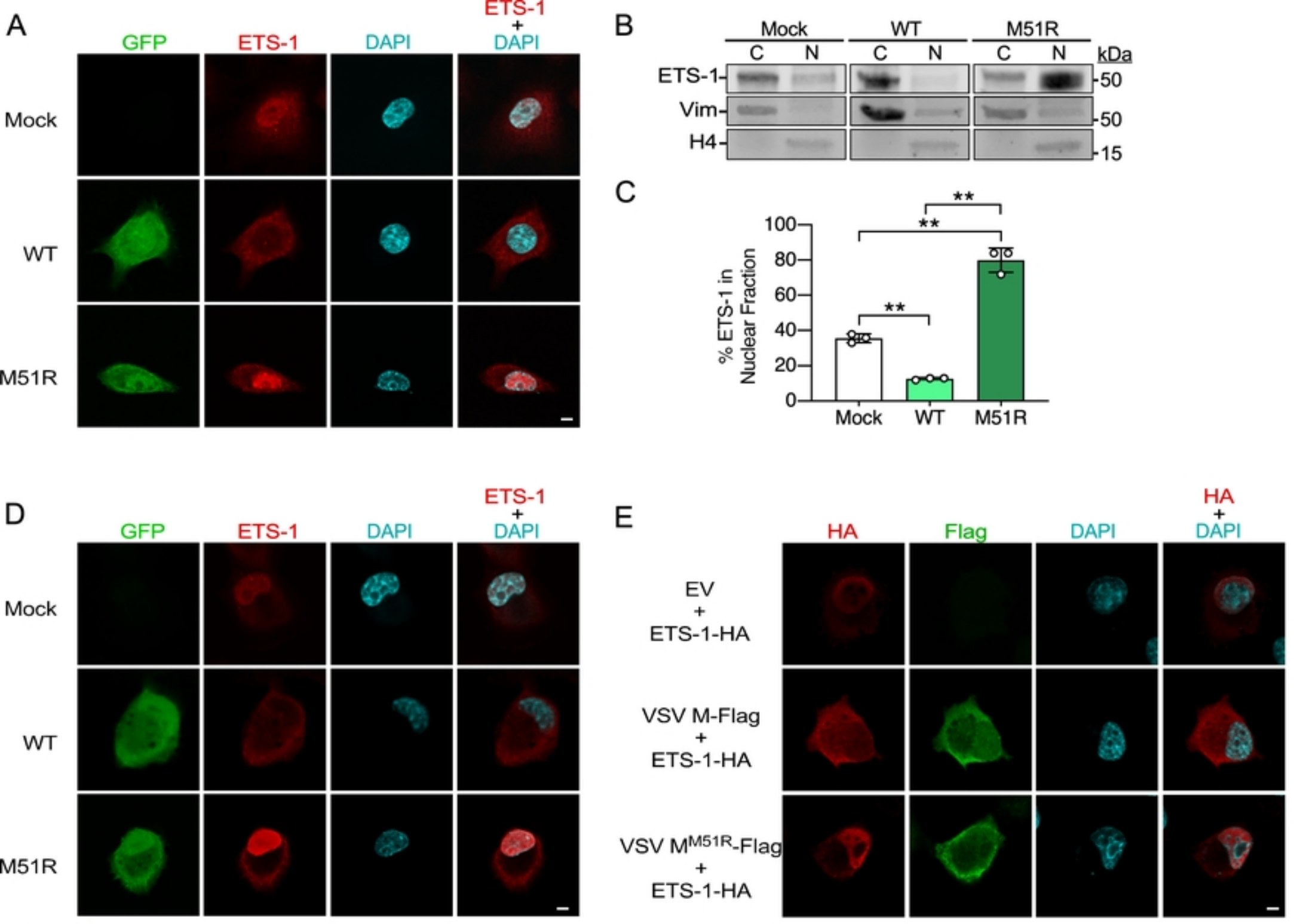
A
GFP
ETS-1
DAPI
ETS-1 + DAPI
Mock
WT
M51R
B
Mock
WT
M51R
C
N
kDa
ETS-1
Vim
H4
50
50
15
C
% ETS-1 in Nuclear Fraction
100
80
60
40
20
0
**
**
**
Mock
WT
M51R
D
GFP
ETS-1
DAPI
ETS-1 + DAPI
Mock
WT
M51R
E
HA
Flag
DAPI
HA + DAPI
EV + ETS-1-HA
VSV M-Flag + ETS-1-HA
VSV M^M51R-Flag + ETS-1-HA

Figure 4

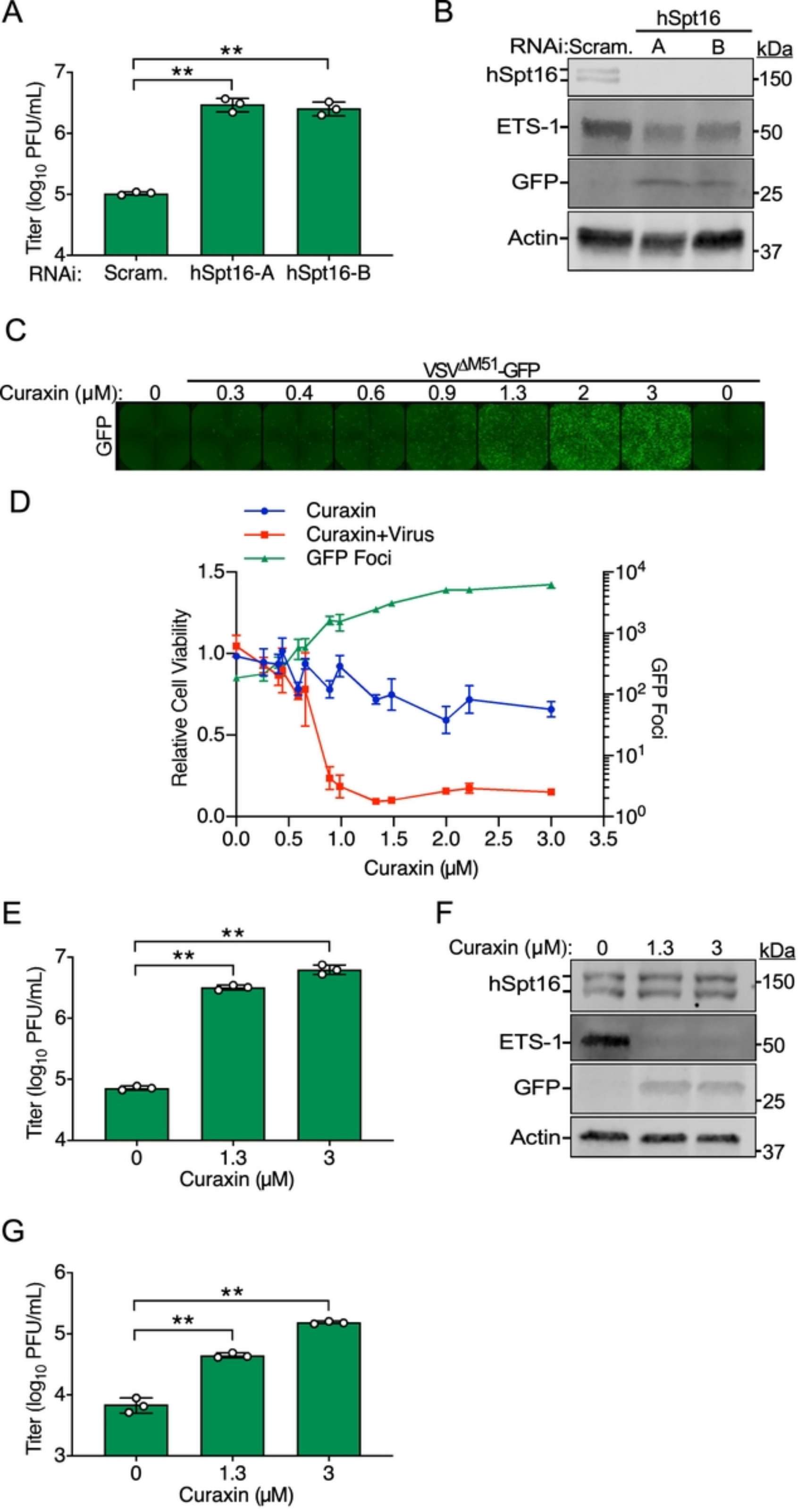
A
Titer (log_{10} PFU/mL)
RNAi: Scram. hSpt16-A hSpt16-B
**
B
hSpt16
RNAi:Scram. A B
kDa
hSpt16
ETS-1
GFP
Actin
150
50
25
37
C
VSV$^{\Delta M51}$-GFP
Curaxin (μM): 0 0.3 0.4 0.6 0.9 1.3 2 3 0
GFP
D
Curaxin
Curaxin+Virus
GFP Foci
Relative Cell Viability
GFP Foci
Curaxin (μM)
E
Titer (log_{10} PFU/mL)
Curaxin (μM)
F
Curaxin (μM): 0 1.3 3
kDa
hSpt16
ETS-1
GFP
Actin
G
Titer (log_{10} PFU/mL)
Curaxin (μM)

Figure 5

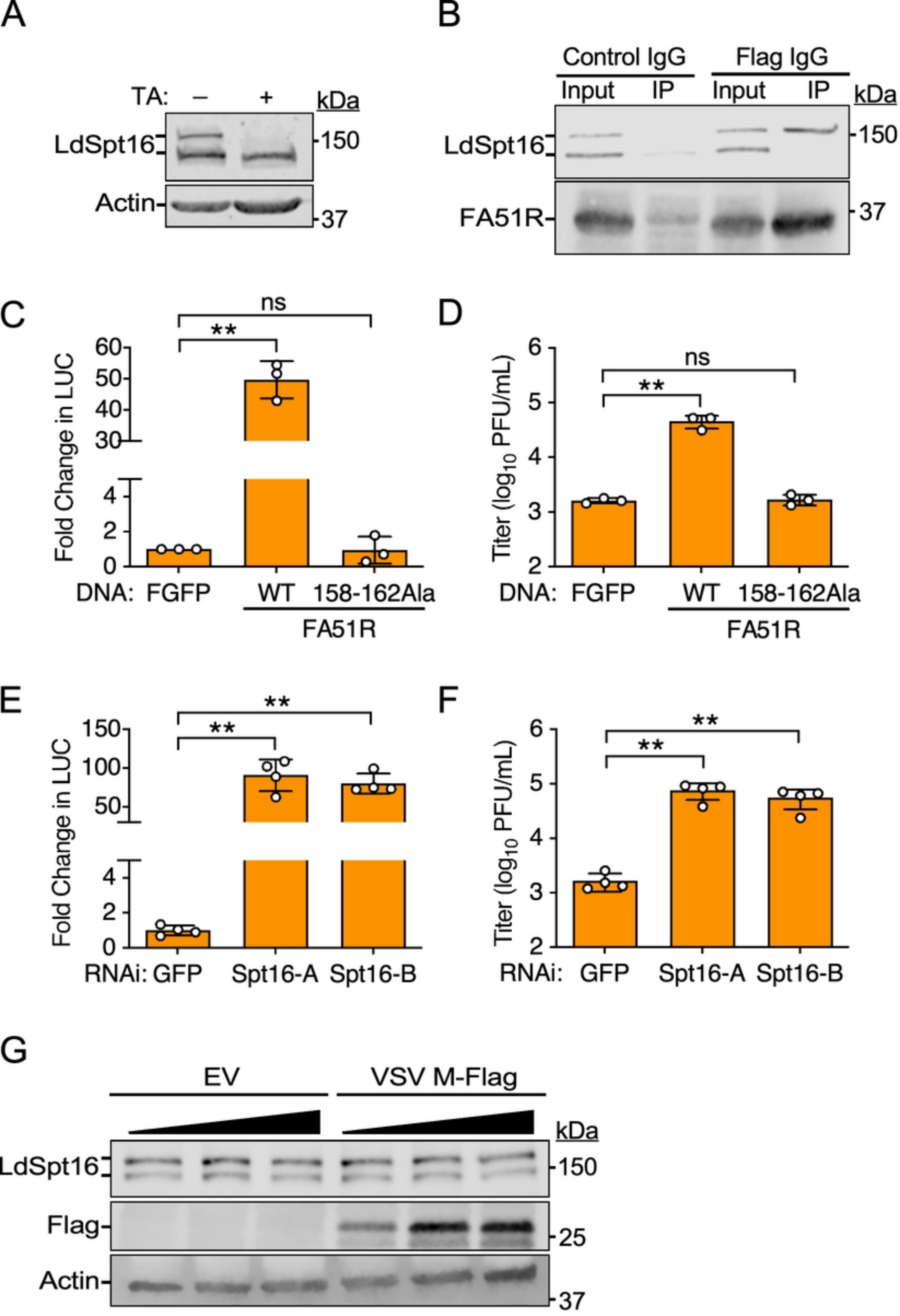
A
TA: – + kDa
LdSpt16
150
Actin
37
B
Control IgG
Flag IgG
Input IP Input IP kDa
LdSpt16
150
FA51R
37
C
ns
**
Fold Change in LUC
60
50
40
30
4
2
0
DNA: FGFP WT 158-162Ala
FA51R
D
ns
**
Titer (log10 PFU/mL)
6
5
4
3
2
DNA: FGFP WT 158-162Ala
FA51R
E
**
**
Fold Change in LUC
150
100
50
4
2
0
RNAi: GFP Spt16-A Spt16-B
F
**
**
Titer (log10 PFU/mL)
6
5
4
3
2
RNAi: GFP Spt16-A Spt16-B
G
EV
VSV M-Flag
kDa
LdSpt16
150
Flag
25
Actin
37

Figure 6

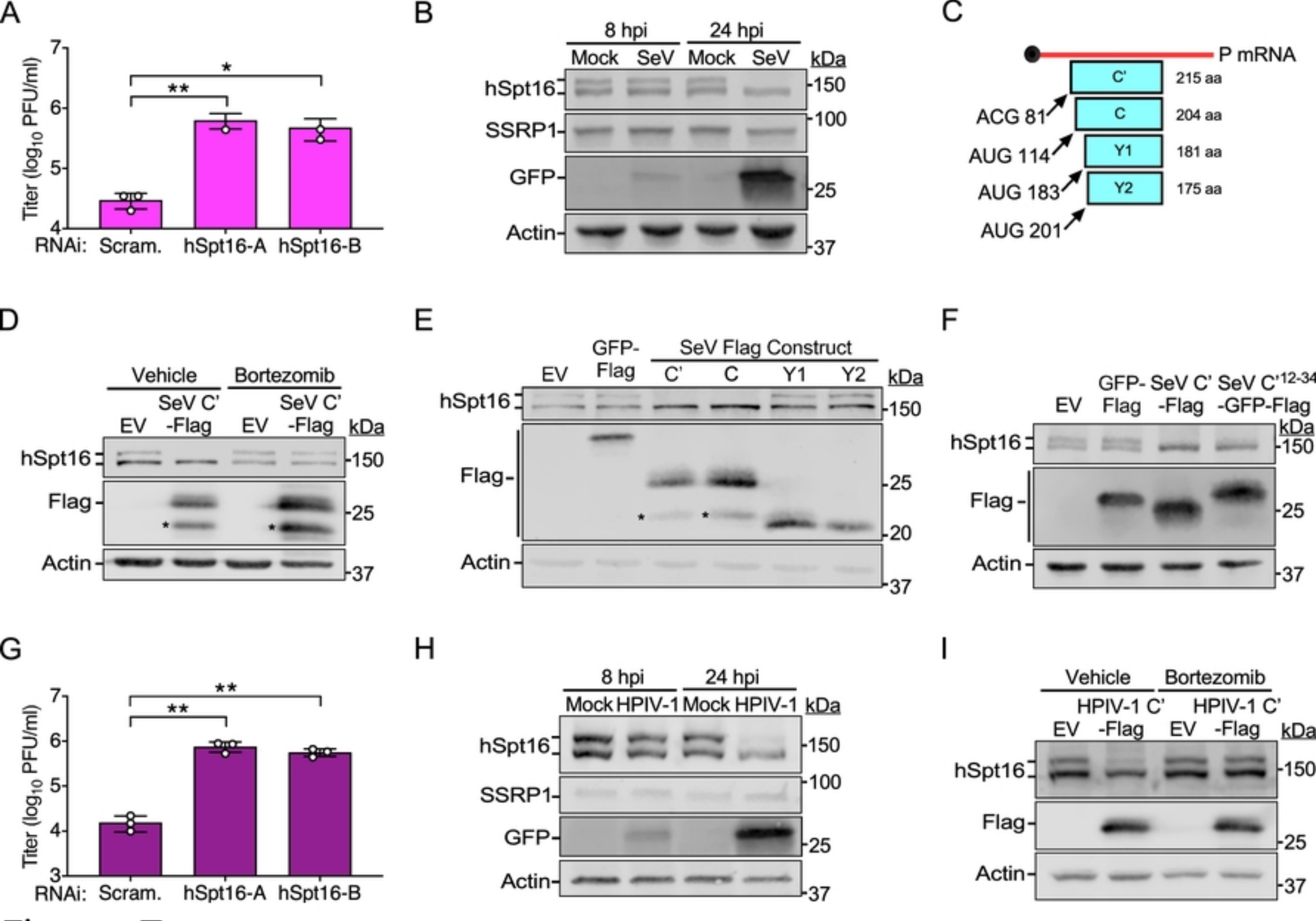
A
Titer (log_{10} PFU/ml)
RNAi: Scram. hSpt16-A hSpt16-B
B
8 hpi 24 hpi
Mock SeV Mock SeV kDa
hSpt16 150
SSRP1 100
GFP 25
Actin 37
C
P mRNA
C' 215 aa
C 204 aa
Y1 181 aa
Y2 175 aa
ACG 81
AUG 114
AUG 183
AUG 201
D
Vehicle Bortezomib
EV SeV C' -Flag EV SeV C' -Flag kDa
hSpt16 150
Flag 25
Actin 37
E
EV GFP-Flag SeV Flag Construct C' C Y1 Y2 kDa
hSpt16 150
Flag 25 20
Actin 37
F
EV GFP-Flag SeV C' -Flag SeV C'12-34 -GFP-Flag kDa
hSpt16 150
Flag 25
Actin 37
G
Titer (log_{10} PFU/ml)
RNAi: Scram. hSpt16-A hSpt16-B
H
8 hpi 24 hpi
Mock HPIV-1 Mock HPIV-1 kDa
hSpt16 150
SSRP1 100
GFP 25
Actin 37
I
Vehicle Bortezomib
EV HPIV-1 C' -Flag EV HPIV-1 C' -Flag kDa
hSpt16 150
Flag 25
Actin 37

Figure 7

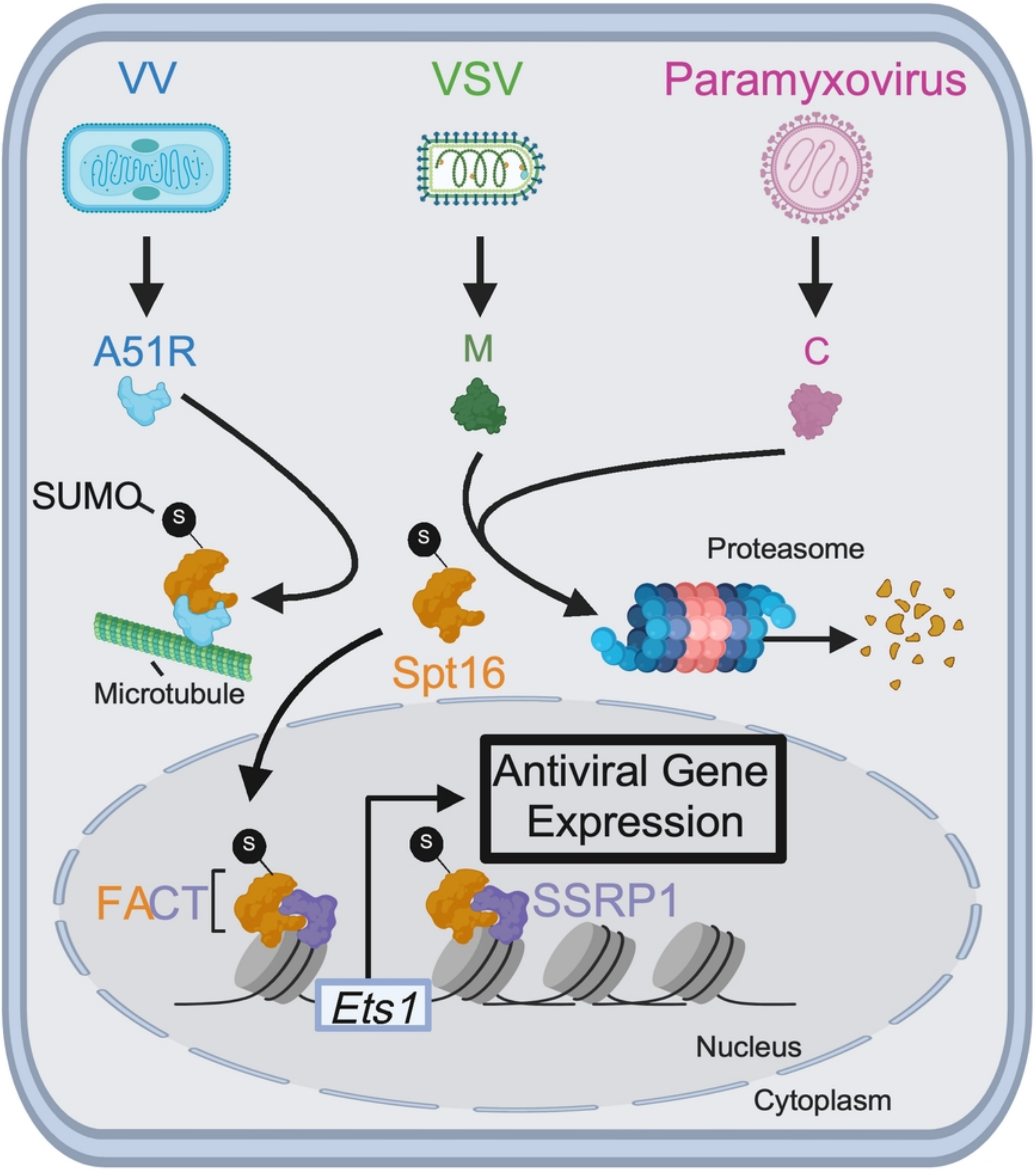
VV
VSV
Paramyxovirus
A51R
M
C
SUMO
S
Proteasome
Microtubule
Spt16
Antiviral Gene Expression
FACT
SSRP1
Ets1
Nucleus
Cytoplasm

Figure 8

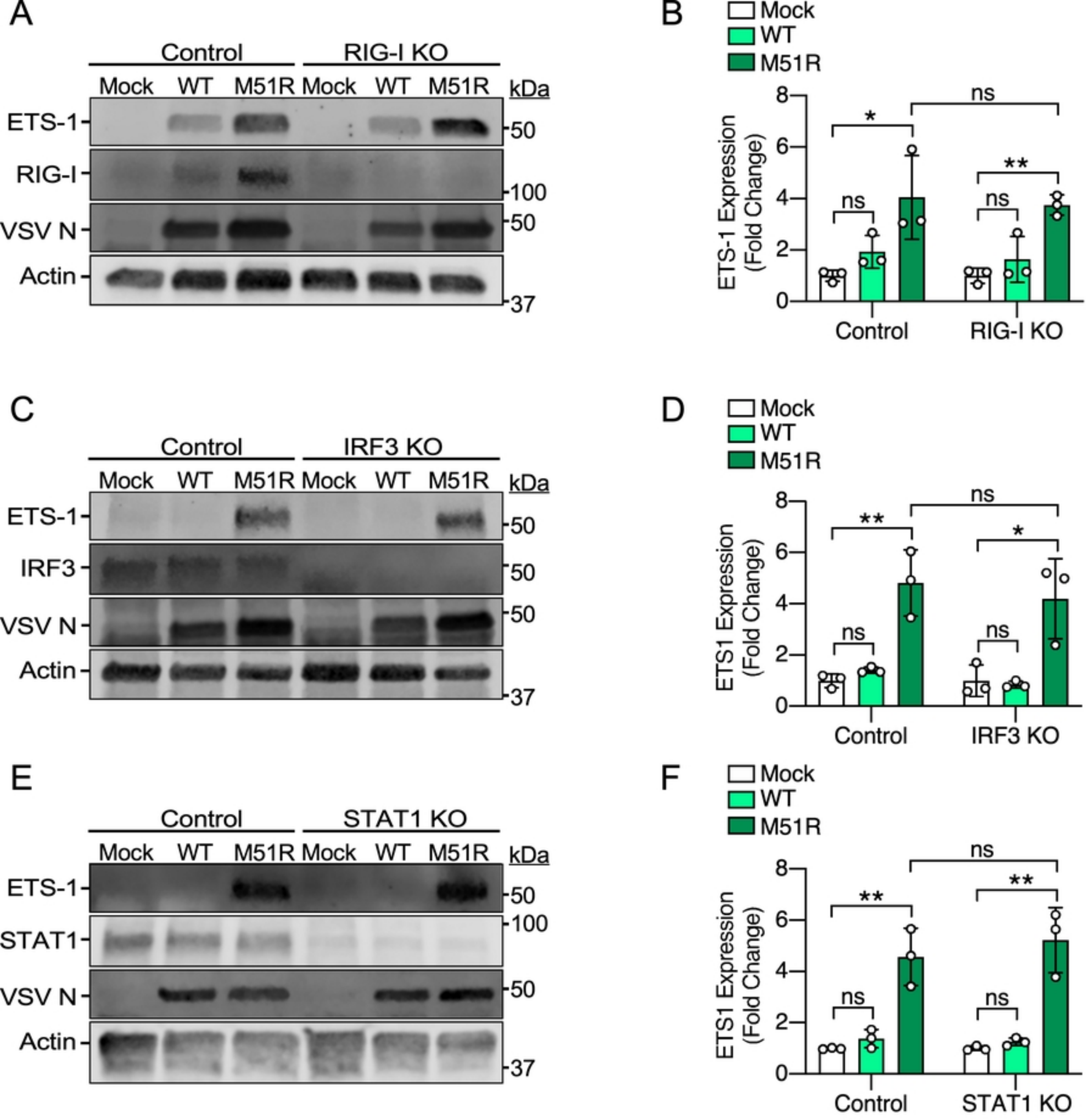
A
Control
RIG-I KO
Mock
WT
M51R
Mock
WT
M51R
kDa
ETS-1
RIG-I
VSV N
Actin
50
100
50
37
B
Mock
WT
M51R
ETS-1 Expression (Fold Change)
ns
*
ns
**
ns
Control
RIG-I KO
C
Control
IRF3 KO
Mock
WT
M51R
Mock
WT
M51R
kDa
ETS-1
IRF3
VSV N
Actin
50
50
50
37
D
Mock
WT
M51R
ETS1 Expression (Fold Change)
ns
**
ns
*
ns
Control
IRF3 KO
E
Control
STAT1 KO
Mock
WT
M51R
Mock
WT
M51R
kDa
ETS-1
STAT1
VSV N
Actin
50
100
50
37
F
Mock
WT
M51R
ETS1 Expression (Fold Change)
ns
**
ns
**
ns
Control
STAT1 KO

Figure S1

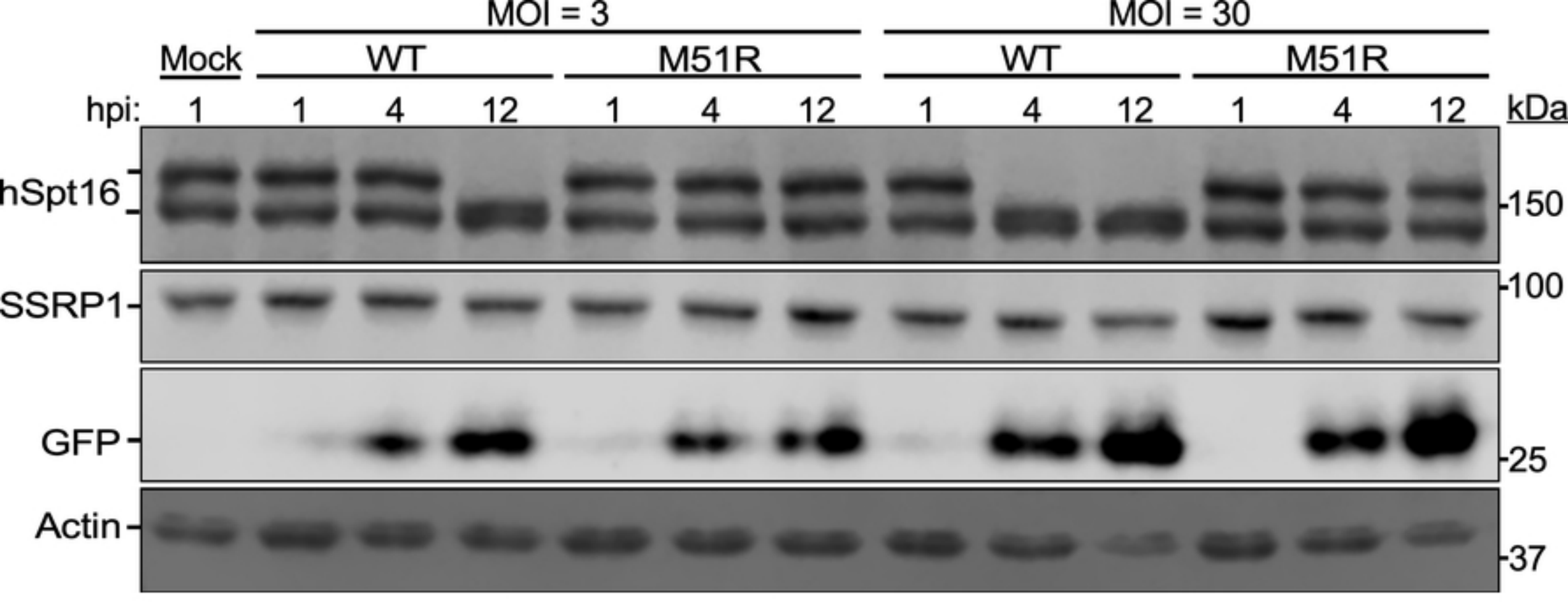
MOI = 3
MOI = 30
Mock
WT
M51R
WT
M51R
hpi:
1
1
4
12
1
4
12
1
4
12
1
4
12
kDa
hSpt16
150
SSRP1
100
GFP
25
Actin
37

Figure S2

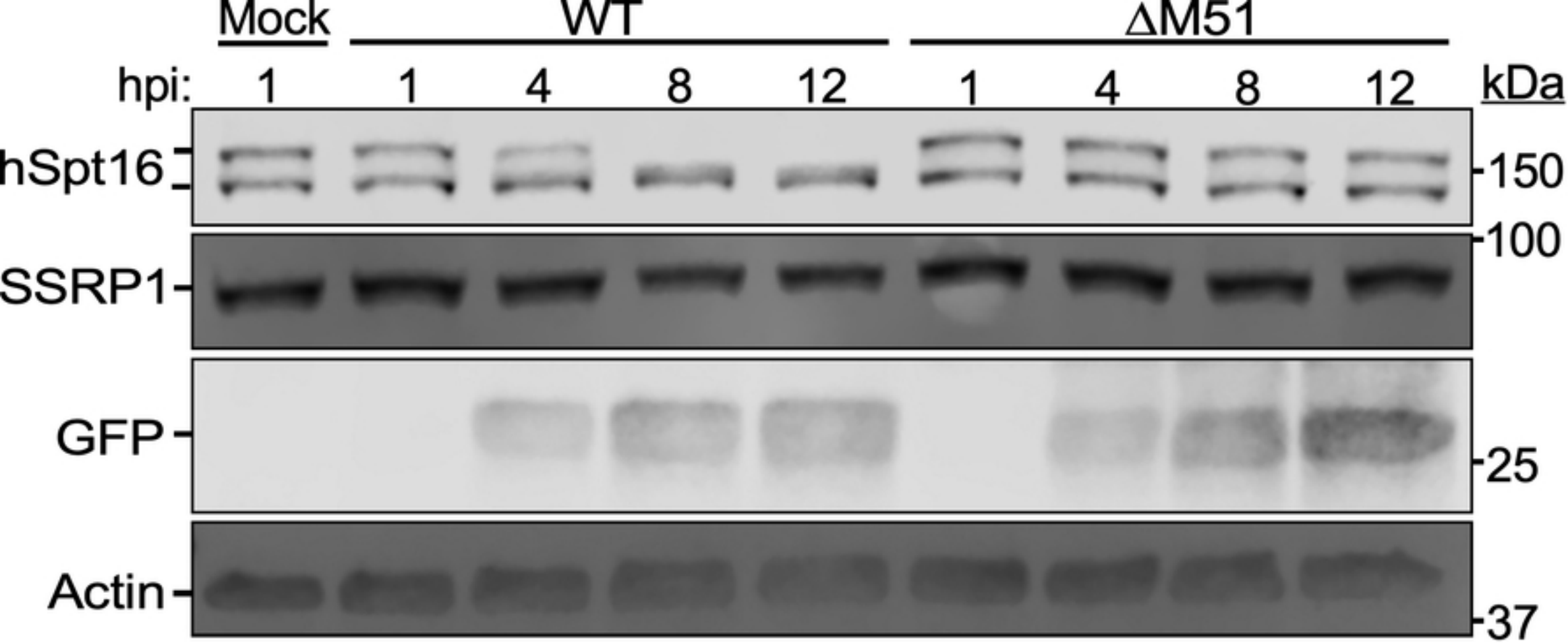
Mock
WT
ΔM51
hpi:
1
1
4
8
12
1
4
8
12
kDa
hSpt16
150
100
SSRP1
GFP
25
Actin
37

Figure S3

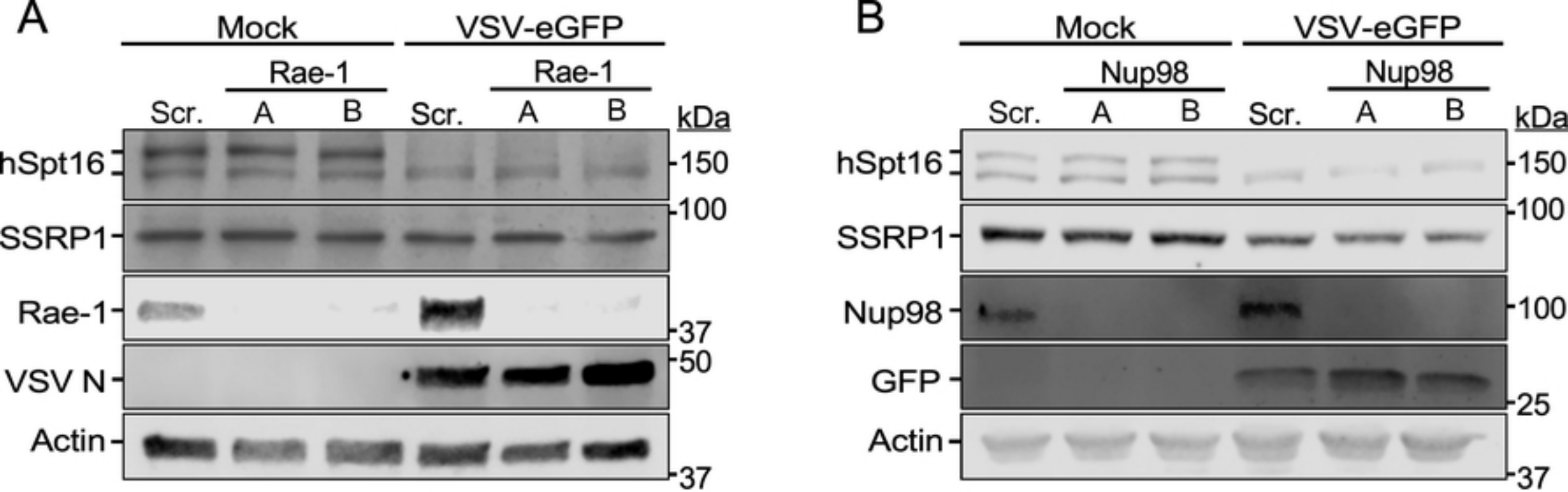
A
Mock
VSV-eGFP
Rae-1
Rae-1
Scr.
A
B
Scr.
A
B
kDa
hSpt16
SSRP1
Rae-1
VSV N
Actin
150
100
37
50
37
B
Mock
VSV-eGFP
Nup98
Nup98
Scr.
A
B
Scr.
A
B
kDa
hSpt16
SSRP1
Nup98
GFP
Actin
150
100
100
25
37

Figure S4

```
        a.a.
hSpt16  758 HDRDDLYAEQMEREMRHKLKTAFKNFIEKVEALTKEELEFEVPFRDLGFNGAPYRSTCLLQPTSSALVNATEWPPFVVTLDEVELI
LdSpt16 761 HDRDDLAAEQSERELRHKLKVAFKSFCERVETMTKQEVEFDTPFRELGFPGAPFRSTVLLQPTSGALVNLTEWPPFVIALEDVELV

hSpt16  844 HFERVQFHLKNFDMVIVYKDYSKKVTMINAIPVASLDPIKEWLNSCDLKY
LdSpt16 846 HFERVQFHLKNFDMVFVFKDYAKKVAMVNAVPMNMLDHVKEWLNSCDIRY
```

Figure S5

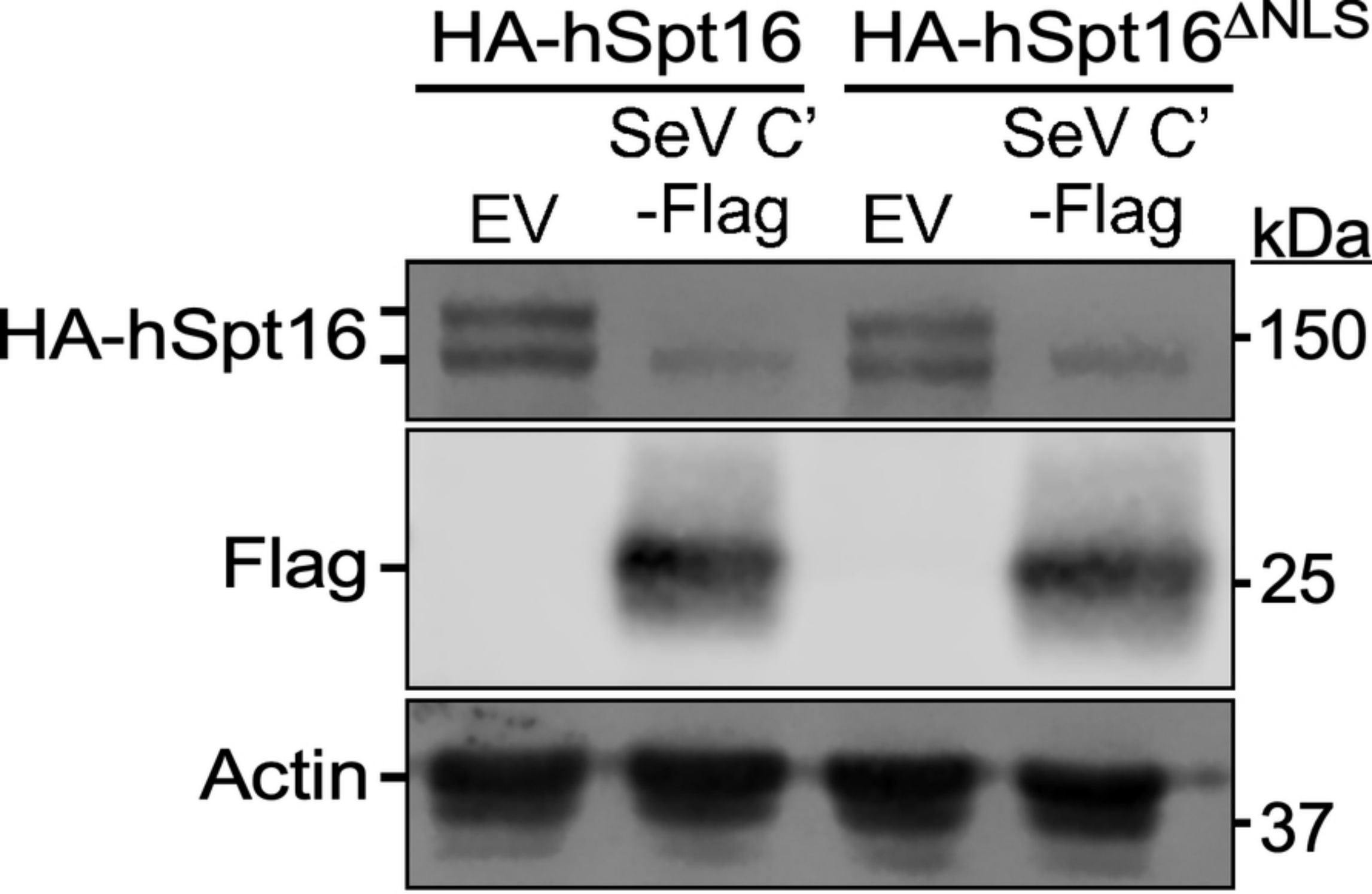
HA-hSpt16
HA-hSpt16ΔNLS
SeV C'
-Flag
EV
SeV C'
-Flag
EV
kDa
HA-hSpt16
150
Flag
25
Actin
37

Figure S6

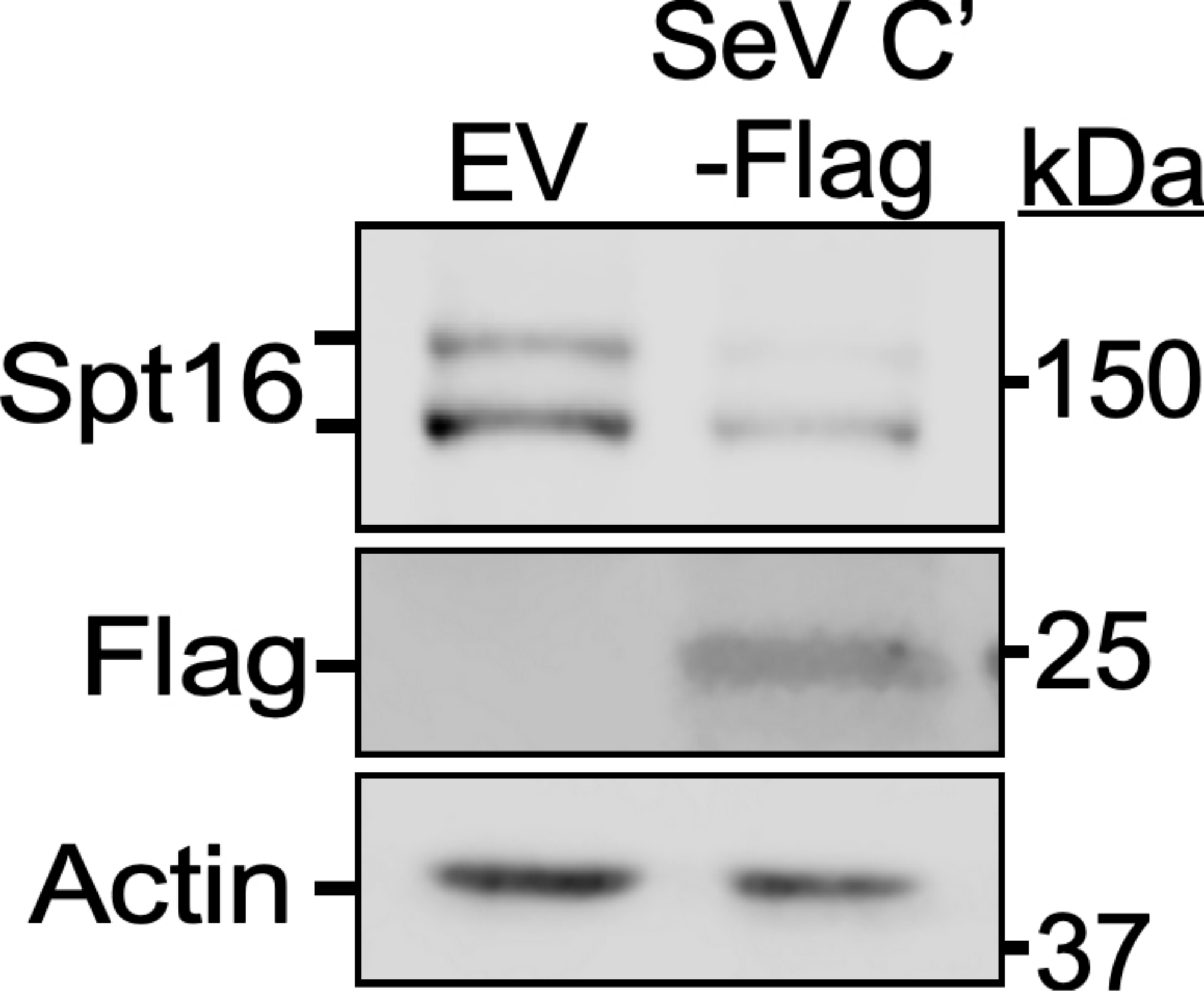

Figure S7

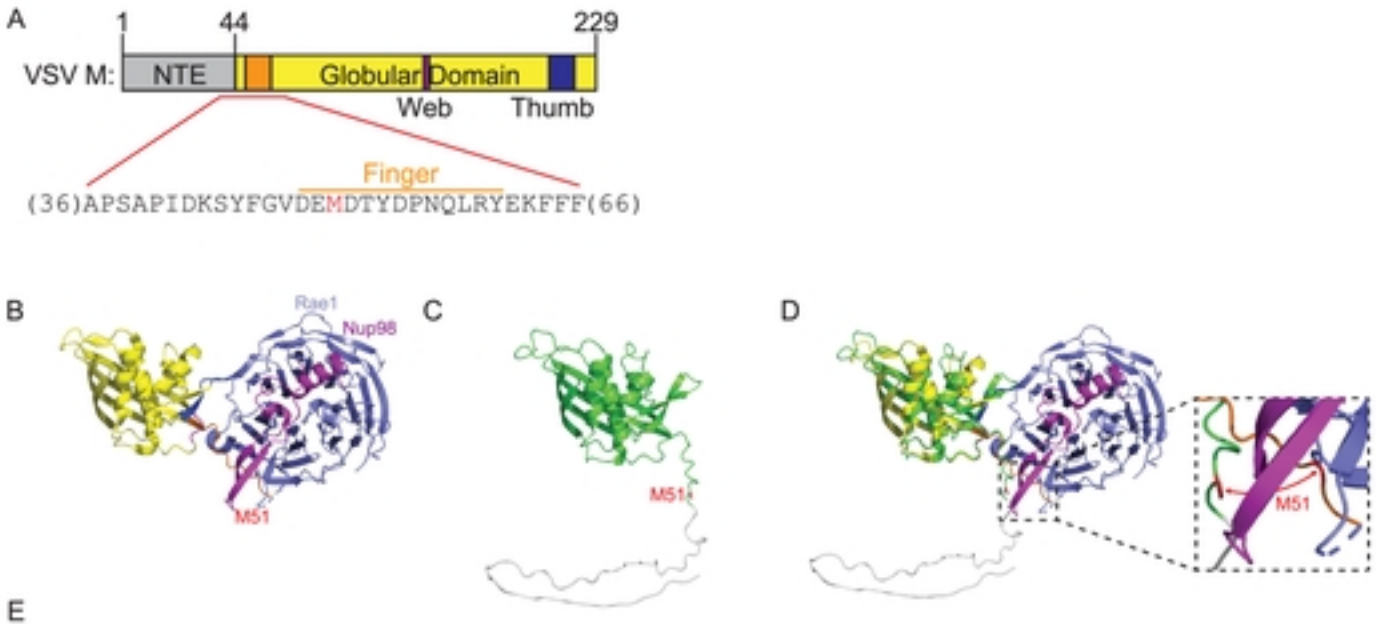

RCSB PDB Pairwise Structural Alignment

Entry	Length	RMSD	TM-Score	Identity	Aligned Residues
VSV M	1-229	0	1	100%	229/229
4OWR	42-229	1.82	0.93	97%	167/188

Figure S8

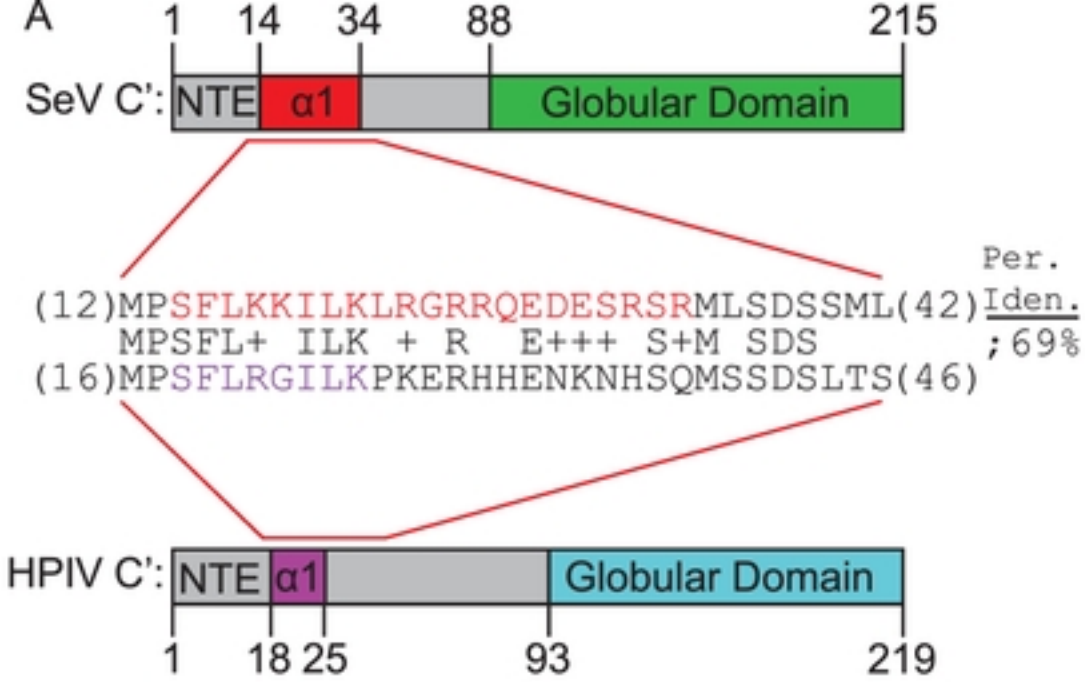

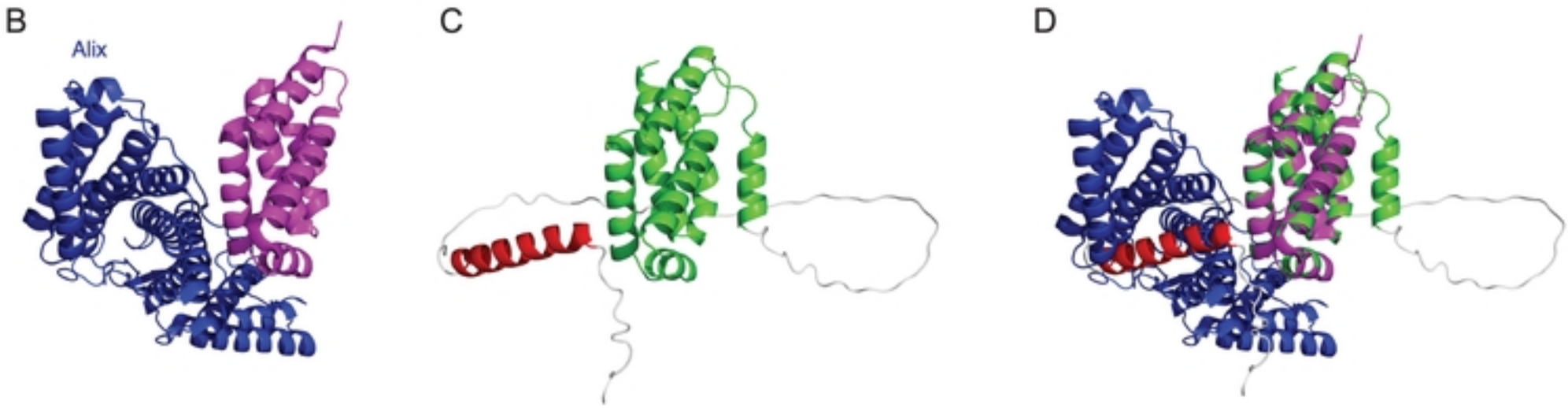

E

RCSB PDB Pairwise Structural Alignment

Entry	Length	RMSD	TM-Score	Identity	Aligned Residues
SeV C'	1-215	0	1	100%	215/215
6KP3	85-215	1.22	0.92	92%	109/119

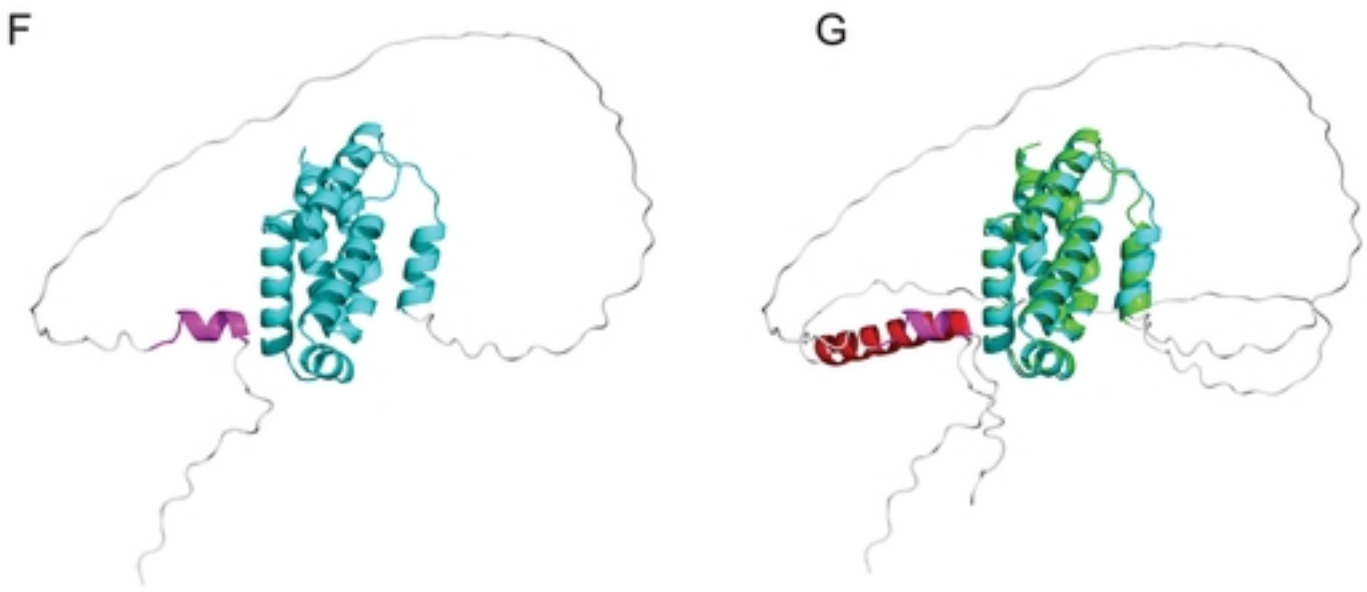

H

RCSB PDB Pairwise Structural Alignment

Entry	Length	RMSD	TM-Score	Identity	Aligned Residues
SeV C'	1-215	0	1	100%	215/215
HPIV-1 C'	1-219	2.57	0.66	77%	144/219

Figure S9

A

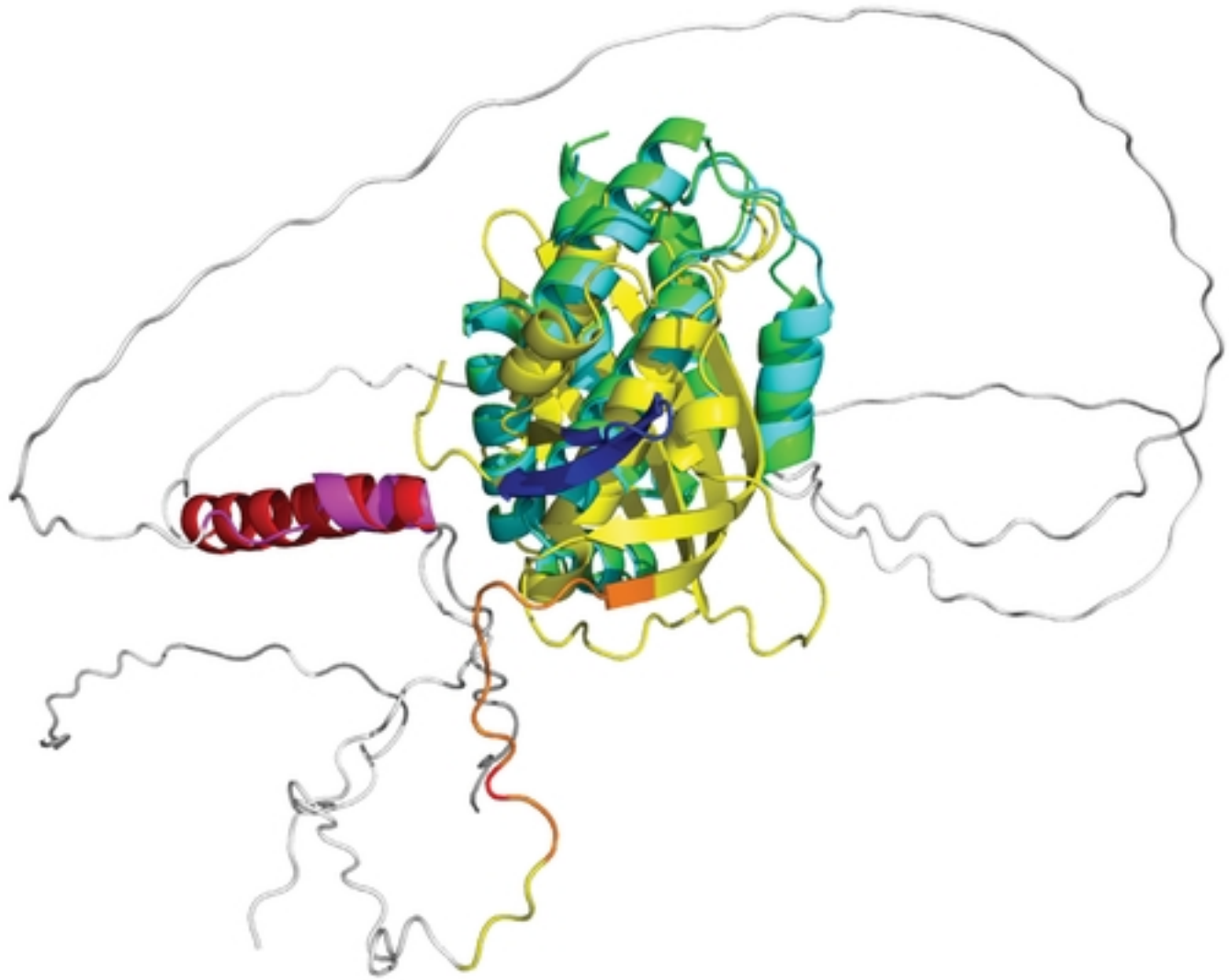

B

RCSB PDB Pairwise Structural Alignment

Entry	RMSD	TM-Score	Identity	Aligned Residues
VSV M	0	1	100%	229/229
SeV C'	5.52	0.22	7%	46/216
HPIV-1 C'	6.45	0.21	5%	43/219

Figure S10